INVESTIGATION OF COUPLING STRATEGIES AND SUBWAVELENGTH FEATURES IN PHOTONIC CRYSTAL CAVITIES FOR OPTICAL MODULATORS

By

Sami Ibrahim Halimi

Dissertation

Submitted to the Faculty of the

Graduate School of Vanderbilt University

in partial fulfillment of the requirements

for the degree of

DOCTOR OF PHILOSOPHY

in

Electrical Engineering

February 28, 2022

Nashville, Tennessee

Committee Members:

Sharon M. Weiss, Ph.D.

Joshua D. Caldwell, Ph.D.

Richard F. Haglund, Ph.D.

Justus C. Ndukaife, Ph.D.

Ronald D. Schrimpf, Ph.D.

To my mom,

whose continual belief in me has kept me going

ACKNOWLEDGEMENTS

Research is full of daily challenges, and it is easy to lose sight of the destination along the way. I would like to extend my gratitude to all of those who have been there with me over the last several years, and without whose support and presence I could not have achieved this. I would like to first thank my family, my mother, and Damion, for always encouraging me and having faith in my ability to succeed. I thank all of my friends who have kept me sane and helped me laugh along the way: Aaron White, Schmelzer, and Zarkota, Tom, Nicole, Shintaro, and many other lovely people who I have had the pleasure of knowing in Nashville and beyond. You know who you are.

Succeeding in graduate school and in the rigors of academic research was not possible without the support of the professors in my committee, including especially my advisor Prof. Sharon Weiss, whom I thank for her guidance throughout my time at Vanderbilt, and Prof. Richard Haglund, whose advice and expertise were indispensable. I also appreciate the mentorship and advice I received from Prof. William Robinson, Prof. Andrew Sternberg, and Prof. Yaqiong Xu. I would like to thank Dr. Shuren Hu, Dr. Kevin Miller, Dr. Kent Hallman, Dr. Josh Fain, and Dr. Francis Afzal, all of whom I appreciate being able to work with and who often graciously gave of their time to help and teach me. I thank Dr. Landen Ryder and Rabeb Layouni for their companionship in the office and Friday afternoon conversations on topics far from the realm of photonics, and thanks also to Dr. Ryan Nolen, who has been a great friend over many years preceding even our time at Vanderbilt. Additionally, I extend thanks to the more junior members of the lab to whom I pass the torch, Josh Allen, Simon Ward, Yanrong Zhang, K.P. Arnold, Juliana Yang, and all the members of the Ndukaife Lab. I give special thanks to Dr. Zhongyuan Fu, Ahsanul Kabir, and Yanrong for sharing their time and working closely with me on several projects.

I have learned so much from everyone and hope I have been able to return that favor in some way. I also thank the brilliant engineers and scientists who worked with me as VINSE staff: Dr. Alice Leach, Dr. Bill Martinez, Dr. Anthony Hmelo, and Dr. Kurt Heinrich.

Finally, I would also like to acknowledge the financial support from the National Science Foundation for funding the work of this dissertation, and the Center for Nanophase Materials Sciences, a DOE Office of Science User Facility, where much of the device fabrication discussed here was carried out. I would like to thank Scott Retterer, Dayrl Briggs, Kevin Lester, and Bernadeta Srijanto for their assistance and levity during my time working with them.

TABLE OF CONTENTS

LIST OF TABLES

LIST OF FIGURES

CHAPTER 1

Introduction

1.1 Optical communication

Current technology is pushing against the demands of our continually growing data needs in the realm of computing. Gordon Moore, co-founder of Intel and Fairchild Semiconductor, observed in the semiconductor industry of the 1960s that computing power was increasing annually as engineers rushed to continually improve computing technologies to meet market demands. His observation, dubbed Moore's Law, that the number of transistors on a single integrated circuit doubles every two years has proven almost prophetic, and the industry has followed this trend closely over the last 40 years. However, as the progression of Moore's Law continues, so too increases the energy requirements for performing that computation. This applies beyond the energy cost for individual logic operations, and the energy consumed by transmitting signals at the interconnections between components can be quite large cumulatively. Transmitting signals over copper at the interconnect scale often presents a bottleneck in performance [1]. With bandwidth usage in telecommunications increasing annually, there is a continual demand in the market for efficient signal processing with high information density, so optical technologies are being employed more. Long-haul telecommunications already rely heavily on fiber optics, and optical interconnects are supplanting electrical interconnects for signals that would be too costly and slow to transmit over electrical lines. Light has been handling the transfer of data between data centers, and now it is more and more handling data within data centers at the inter-chip and even intra-chip level [2,3]. In this way, optical solutions to signal transmission could enable low-energy (sub-femtojoule) information processing while also providing for high information density in an architecture that interfaces directly with the long-haul communications standards in use today [1].

In addition, perpetually reducing transistor sizes poses practical difficulties as the physical structures cannot be miniaturized infinitely, and quantum mechanical effects become harder to mitigate as we push beyond the MOSFET gate sizes of current state-of-the-art nodes (3-nm process as of this year [4]). While the current approach being taken by the industry is to develop more sophisticated computer architectures and transistor geometries to increase computational power without requiring higher transistor density, these challenges have motivated researchers, both in industry and academia, to investigate alternative technologies to the current semiconductor transistor that may offer advantages in specific use cases. While none of these alternatives have supplanted the traditional transistor in terms of device footprint and energy per logic operation [5], this pursuit has yielded much new knowledge about switching platforms and increased our understanding of the physical systems involved. One such direction of pursuit is to develop an "optical transistor" that can switch signals at optical frequencies. Though it would not replace the transistor in classical computing, due to the potential for multiplexing signals across a wide range of light frequencies to achieve high-bandwidth operation with low-loss transmission even at high data rates, performing computation in the optical regime with an optical transistor in a photonic platform is seen as a valuable approach to extend upon our already robust capabilities in traditional computing and expand into new domains. This includes direct integration of optical logic alongside other optical or optoelectronic components (e.g., optical modulators, sensors, or photodetectors), cases where logic operations might be separated by large distances [5], and leaning into quantum effects by implementing quantum logic at single-photon levels [6].

1.2 Optical modulators and photonics

Silicon photonics as a field is expanding as it is investigated as a solution to our future information needs. Optical modulators relying on silicon photonics platforms promise high-bandwidth, low-power operation without significant concern of cross-talk between channels. With a photonic platform, the electrical signals in data centers are replaced with light pulses. Optical circuitry, built upon robust light sources, signal routing, and photo-detection, requires high-performance optical modulators to encode information, perform switching, and even potentially enable computation with light. Integrated silicon photonics follows the traditional electronic paradigm and embeds many of such devices onto a chip to form "photonic integrated circuits."

There are a wide variety of techniques and processes that can be used to modulate the amplitude, phase, and polarization of light, and which strategy gets applied depends largely on the material system being used and what trade-offs are deemed to be more palatable in terms of speed, energy requirements, and other fundamental physical limitations. Important metrics to consider when comparing the performance of modulators are bandwidth, speed, and device footprint [2]. High-performance optical modulators must also have low insertion loss, which quantifies the amount of loss incurred by simply inserting the device into the signal path; modulation depth, which indicates the ratio (in dB) of maximum to minimum intensity; and energy per bit, which is related to the energy efficiency and heat generation of the modulator.

Overall, the field of silicon photonics has made great developments in recent decades toward these goals in data processing and signal modulation, and CMOS-compatible photonic devices have the potential to be readily integrated into foundry processes and interfaced with existing optoelectronics. The silicon photonics platform is also being considered for optical

computing [5], and, in single-photon regimes, quantum computing and quantum information processing become engaging possibilities [7].

1.3 Waveguides

The foundational structure of integrated photonics is the optical waveguide. In the analogy between integrated photonics and integrated electronics, the waveguide performs for light the function performed by a trace or wire for electrical signals. That is to say that an integrated waveguide carries optical signals across distances within a photonic integrated circuit. Several more complicated photonic structures directly build upon the waveguide, as will be discussed later. The optical waveguide is able to confine and propagate light due to total internal reflection [8]. Reflections occur at the interfaces between the high-index waveguide medium and the low-index cladding medium surrounding it, and for light incident on the interface at selected angles above a critical angle, defined as $\theta_c = \arcsin(n_2/n_1)$, the wave is reflected back into the structure and continues to reflect at subsequent interfaces and propagate down the length of the waveguide. This results in a guided optical mode, whose effective index is determined by the geometry and composition of the waveguide. There exist different types of waveguides with differing geometries. In fact, an optical fiber is itself the most well-known type of waveguide, though here we shall direct our focus to the on-chip varieties. Among these are the planar waveguide, the rib waveguide, and the buried channel waveguide, though we focus on the ridge waveguide, which consists of a rectangular block of high-index material sitting atop a substrate cladding of lower index. In the work shown in this dissertation, the waveguide is made of silicon and the substrate of silicon dioxide, and the upper cladding is air. Figure 1.1(a) shows a schematic illustration of a ridge waveguide geometry.

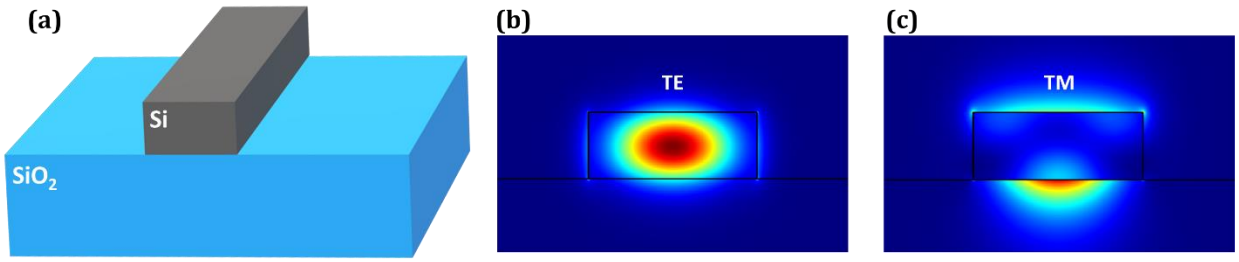

Figure 1.1. (a) Schematic illustration of a basic ridge waveguide structure made on a silicon-on-insulator (SOI) platform. (b, c) Simulated TE (a) and TM (b) modes of a simple SOI ridge waveguide.

The ridge waveguide, depending on the dimensions and material of the waveguide geometry, can support a variety of optical modes, characterized as electromagnetic modes of the form $E(x,y)e^{i(-\omega t+\beta z)}$ where z is the direction of propagation [8]. The polarization of these modes is often discussed according to the orientation of the electric and magnetic field components relative to the plane of incidence of the wave, using the conventions transverse electric (TE) or transverse magnetic (TM). For a mode with TE polarization, the electric field oscillations are perpendicular (transverse) to the plane of incidence, and conversely, for a TM mode, the magnetic field is perpendicular. Figure 1.1(b,c) provide example 2D spatial profiles of TE and TM modes for a ridge waveguide. The effective index of the mode defines its velocity within the waveguide, which differs from the bulk index due to the dispersion brought about by the waveguide geometry:

$$n_{eff} = \frac{c}{\omega}\beta = \frac{\beta}{k_0} \tag{1.1}$$

Here, β represents the wave vector of the mode. Note also that there exists an evanescent component that permeates outside the extent of the waveguide structure. This evanescent wave plays an important role in different optical coupling strategies, as we will discuss in Chapter 2.

Generally, a TE mode will have a larger evanescent wave at the lateral interface of the waveguide due to the direction of the electric field polarization, whereas a TM mode will have greater permeation into the low-index cladding below and the air above.

1.4 Photonic crystal theory

1.4.1 Introduction to photonic crystals

The microelectronics industry is built upon the crystalline properties of semiconductors, such as silicon, whose regular atomic arrangement produces an electronic band gap, a range of energies disallowed in the crystal. This band gap is then engineered, by adding dopants to the material, to produce the assortment of semiconductor devices – diodes, transistors, etc. — that enable our electronic world.

Within the realm of silicon photonics, one of the powerful tools at our disposal is the photonic crystal, an optical analog to atomic crystals that similarly produces a range of disallowed energy states, however for photons instead of electrons [9]. Much of the same mathematical formalism used to model the quantum mechanical dynamics of electrons in crystals can be applied to model the electrodynamics of a photonic crystal. The photonic band gap, achieved by periodically varying refractive index, provides a way to control the propagation of light and engineer the diffraction, reflection, and confinement of optical fields. Figure 1.2(a) shows example band structure plots and the band gap brought about by alternating refractive index values in a multilayer film. The greater the index contrast between the high and low index regions, the larger the band gap that is created.

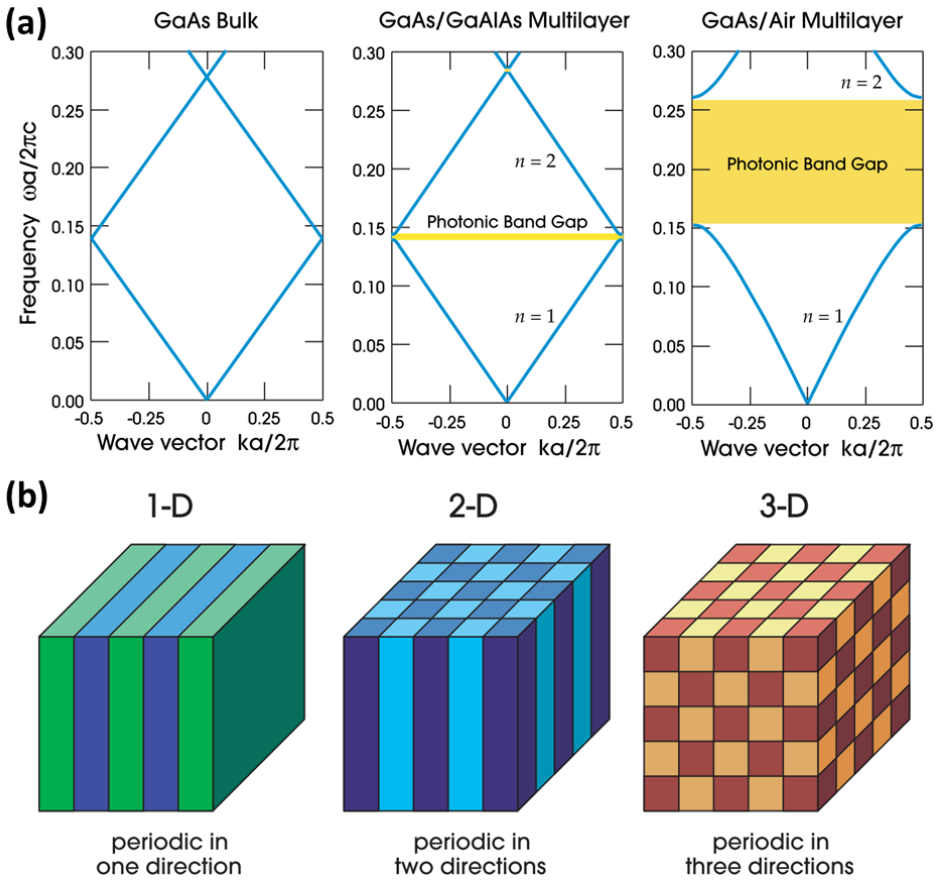

Figure 1.2. (a) Band diagrams for a multilayer film showing the creation of a photonic band gap by periodically alternating refractive index, with a larger index contrast producing a larger band gap. (b) Potential dimensionality of photonic crystal periodicity. Reprinted with permission from [9], © 2008 Princeton University Press.

Photonic crystals can be constructed with one-, two-, or three-dimensional periodicity (Fig. 1.2(b)), though three-dimensional photonic crystals pose fabrication challenges in many material systems. Within the scope of silicon photonics and optical modulators, it is often desirable to fabricate photonic crystals using CMOS-compatible processes or, at the very least, somewhat scalable processes, which imposes certain limitations on the length scales and dimensionality of periodicity that are achievable. Fortunately, in many applications 1-D photonic crystals will suffice. For example, by introducing a defect state within a photonic band gap, an optical cavity (or resonator) can be created with a photonic crystal. In the 1-D case, this is accomplished by breaking

the translational symmetry with an added layer of different thickness or refractive index. This will be the topic of more detailed discussion in Section 1.4.2.

Figure 1.3 shows an example of a 1-D PhC embedded into a waveguide, and the band structure of this device. Pulling from the Bloch Theorem, the periodicity of the PhC modulates the wave vector of the guided mode that is travelling through the waveguide. This is seen in how the PhC wave vector, k, relates to the vacuum wave vector, k_0:

$$k = k_0 n_{eff} = \frac{2\pi}{\lambda} n_{eff} \tag{1.2}$$

$$\omega = \frac{c}{n_{eff}} k \tag{1.3}$$

The frequency of the mode is thus related to the wave vector, being scaled inversely by the effective index. A higher effective index for the mode implies a smaller frequency (or a longer wavelength). A band diagram can describe the relationship between the frequency and wave vector of light in a PhC and reveal the presence of photonic band gaps, as shown previously in Fig. 1.2(a).

In analogy to the valence and conduction band of a semiconductor band gap, a PhC possesses dielectric and air bands at the edge of its band gap. These band edges inform us about where the energy density of the modes is localized within the PhC structure. At the dielectric band edge, the energy is localized in the high-index region of the PhC (between the air holes), while the air band edge has energy localized inside the low-index region (inside the air holes). These modes arise at the edge of the irreducible Brillouin zone, at $k_x = 0.5\ (2\pi/a)$, as a consequence of the inherent symmetries of the electric field in that mode since it must align with the periodicity of the structure.

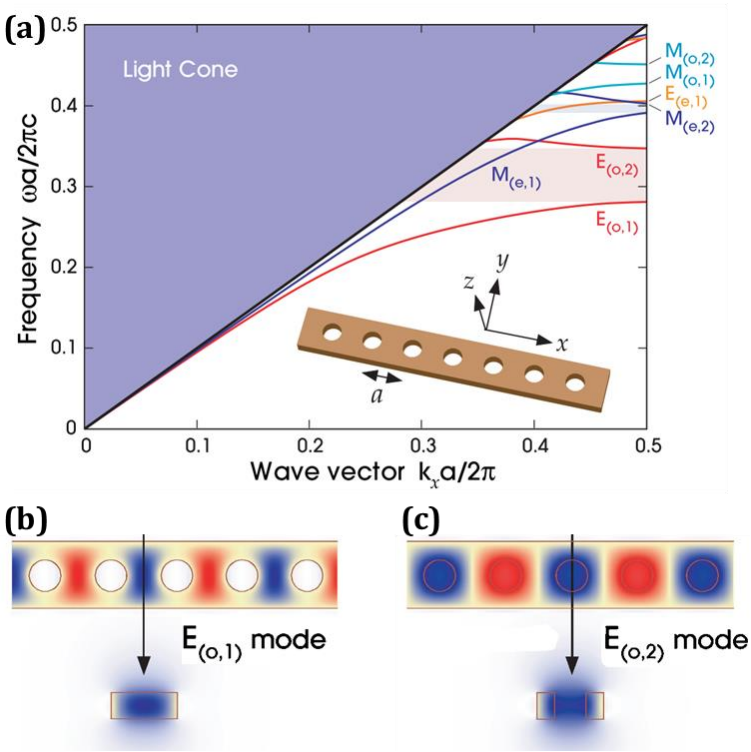

Figure 1.3. (a) Band diagram for a 1-D photonic crystal embedded into a waveguide, showing the existence of several bands within the irreducible Brillouin zone. (b, c) Mode profiles for the dielectric band edge (b) and the air band edge (c). Figures reprinted from [9], © 2008 Princeton University Press.

1.4.2 Photonic crystal nanobeam cavities

Extending from this simplest photonic crystal system, we can consider drilling out a periodic array of air holes into an on-chip optical waveguide, utilizing the total internal reflection for confinement at the cladding interfaces and employing this 1-D photonic crystal for confinement in the direction of propagation. This structure is known as a PhC nanobeam cavity. Just as a Fabry-Pérot or laser cavity confines light between two reflective mirrors, the band structures of each unit cell in a PhC nanobeam are careful tailored so that the desired resonance wavelength of the cavity is reflected at the outer unit cells by their band gap. An optical cavity made in this way is capable of generating resonant modes that can interact with other in-plane guided modes. Figure 1.4 shows a representative band diagram and mode profile for this sort of PhC.

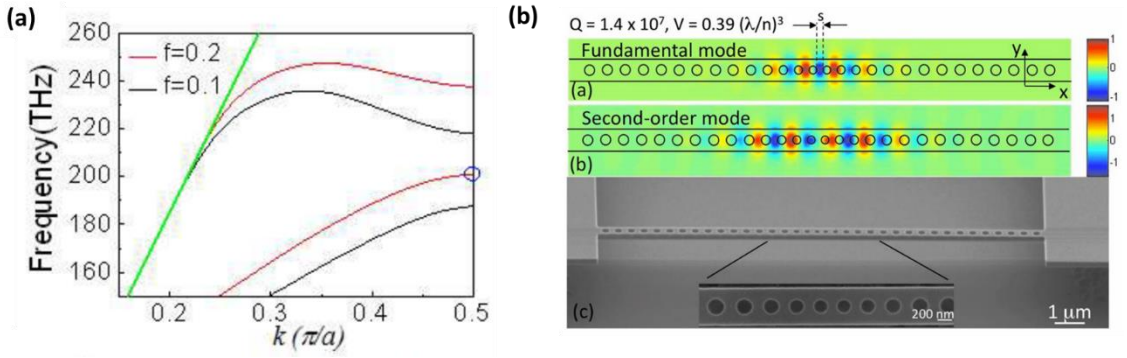

Figure 1.4. (a) Band diagram for a PhC nanobeam cavity, where the resonance (blue circle) is at the lower-frequency band edge of the cavity unit cell (red curves), which is a defect state lying within the band gap of the surrounding mirror unit cells (black curves). Reprinted from [10], © 2011 Optica Publishing Group. (b) Electric field mode profiles for the fundamental and second-order modes in a fabricated, suspended PhC nanobeam. Reprinted with permission from [11], © 2009 AIP Publishing.

To discuss the performance of a PhC nanobeam cavity, we can characterize a resonant mode of the cavity in terms of its temporal confinement (quality factor, or Q) and spatial confinement (mode volume, or V_m). The quality factor, itself a dimensionless unit, effectively informs us about the lifetime of a photon in a PhC cavity or, likewise, the ratio of optical energy stored (U) to the rate of energy dissipation out of the cavity (P) at a particular frequency (ω_0):

$$Q = \frac{U}{P}\omega_0 \tag{1.4}$$

We model these resonant peaks in transmission as a Lorentzian function, and the Q can be calculated by observing the linewidth of a resonance in the transmission spectrum as $Q = \lambda_0/\Delta\lambda$ where $\Delta\lambda$ is the full-width half-maximum (FWHM) of the curve. The mode volume, as we define it when discussing PhC cavities, is calculated by integrating the electric field energy density over the volume and normalizing it by the maximum value [12]:

$$V_m = \frac{\int \varepsilon |E|^2 dV}{\max\left(\varepsilon |E|^2\right)} \tag{1.5}$$

These PhCs can efficiently confine light at the wavelength scale – and smaller, as we will see – to provide enhancement of the optical field and filtering of signals.

1.4.3 Subwavelength features for enhanced light-matter interaction

Light-matter interaction is a requirement for many useful applications of photonics built upon absorption, emission, or transmission of light. These interactions often demand high electric field strength for maximum efficiency, and in many cases, scale with Q/V_m. We have previously reported a PhC nanobeam cavity with a dielectric "bowtie" unit cell geometry that is capable of deep-subwavelength confinement of light with remarkable electric field enhancement [13,14]. It is worthwhile to discuss the bowtie PhC to examine its operation in detail, as the intuition derived therein explains the usage of all the subwavelength features dealt with in this work and motivates their use in modulator applications. Commonly investigated optical resonators have achieved high Q, as is the case with low-loss, dielectric cavities, or low V_m, such as with plasmonic resonators, but realizing high Q/V_m requires simultaneously overcoming Ohmic losses and the diffraction limit. The bowtie PhC cavity allows for resonant modes with high temporal and spatial confinement (i.e. large Q/V_m) by leveraging the interface conditions of Maxwell's equations to further confine light in a high-Q photonic crystal nanobeam cavity.

Related to the bowtie geometry is the antislot unit cell, which is a simple demonstration of this subwavelength mode concentration that can act as a theoretical basis for exploring the operation of the bowtie. The slot effect [15] has been explored in PhC nanobeams [16,17] as a means for concentrating light into a narrow, low-permittivity slot in a high-permittivity structure, as shown in Fig. 1.5(a,b). We can describe this effect mathematically by considering the normal

component of the electric displacement field at the interface between the slot region and the adjacent high-permittivity region (subscript 1).

$$\hat{n} \cdot \left(\vec{D}_1 - \vec{D}_{slot}\right) = \sigma \tag{1.6}$$

Where $\hat{n}$ represents the unit normal vector of the interface, and σ is surface charge density. If there exists no surface charge, the normal component of the displacement field is continuous across this interface.

$$D_{1,n} = D_{slot,n} \tag{1.7}$$

$$\varepsilon_{high} E_{1,n} = \varepsilon_{low} E_{slot,n} \tag{1.8}$$

$$E_{slot,n} = \frac{\varepsilon_{high}}{\varepsilon_{low}} E_{1,n} \tag{1.9}$$

This results in an enhancement of the electric field in the slot region by a factor of $\varepsilon_{high}/\varepsilon_{low}$. This enhancement factor also acts to increase the electric field energy density, $u = \frac{1}{2}\vec{E} \cdot \vec{D}$. The antislot effect operates by similar principles, squeezing light into a high-permittivity region with high electric field energy density locally in the antislot [13]. In this case, the tangential component of the electric field is continuous across the interface between the antislot and an adjacent low-permittivity region, requiring the field to be polarized such that it is parallel to the antislot.

$$\hat{n} \times \left(\vec{E}_1 - \vec{E}_{slot}\right) = 0 \tag{1.10}$$

$$E_{1,t} = E_{antislot,t} \tag{1.11}$$

$$D_{antislot,t} = \frac{\varepsilon_{high}}{\varepsilon_{low}} D_{1,t} \tag{1.12}$$

In a PhC nanobeam, the antislot effect can be applied to enhance the field within the unit cells by introducing a dielectric bar into the air hole. For a nanobeam cavity designed for TE-polarized, air-mode resonance, a dielectric bar placed perpendicular to the direction of propagation allows

for increased electric field energy density and further concentrates the light beyond the mode confinement due to high-Q cavity resonance.

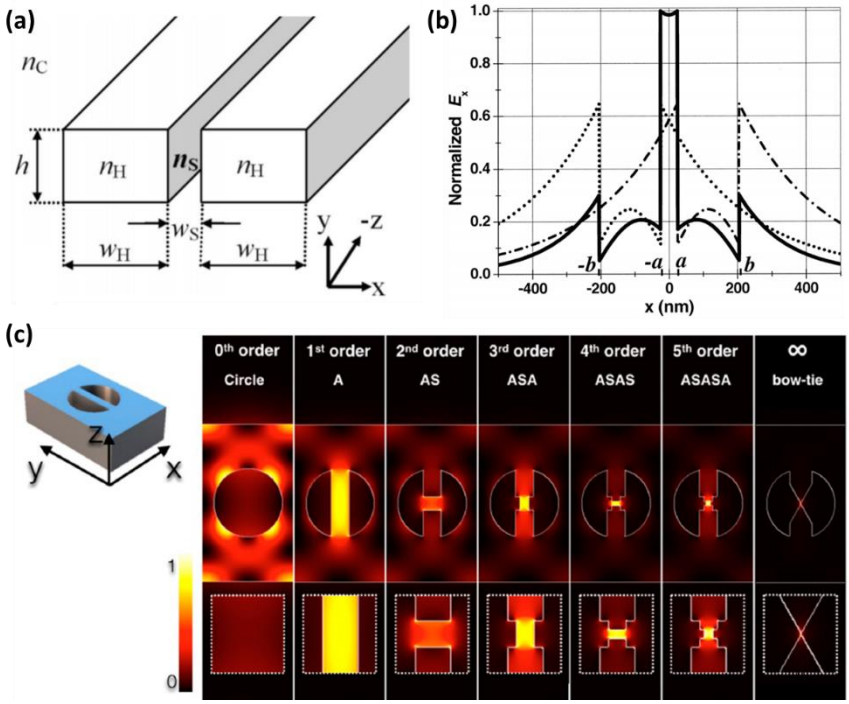

Figure 1.5. Overview of slot and antislot effects. (a) Schematic illustration of a slot waveguide and (b) the enhancement of the electric field within the low-permittivity slot region. Figures reprinted from [15], © 2004 Optica Publishing Group. (c) Extreme confinement of light achieved by interlocking slots and antislots within the air-hole unit cell of a 1-D photonic crystal nanobeam, resulting in a bowtie geometry at the limit [13]. The second row of field profiles are zoomed-in images of the first.

Interestingly, incorporating the slot and antislot geometries together enables field enhancement from both complementary effects. By adding a slot region into an antislot and, from there, a smaller antislot into that nested slot (and so on), we can imagine the confined light being squeezed further and further down [13,14]. Figure 1.5(c) shows the sequence of these interlocked designs and the progressive focusing of light afforded by it, which results ultimately in a bowtie geometry at the limit.

This bowtie design, as well as the simple antislot geometry, effectively serve to reduce the mode volume for the PhC nanobeam's resonance. The mode volume, as defined in Eq. 1.5, reveals the peak electric energy density of the mode in question, which is boosted by the presence of these subwavelength features. Design guidelines already exist for realizing PhC nanobeam cavities with ultrahigh Q [10,18]. When embedded into a carefully designed PhC nanobeam cavity, the bowtie unit cell geometry becomes a powerful tool for increasing Q/V_m and enabling advanced light-matter interaction. The mix-and-match design technique discussed in Chapter 3 further simplifies the practical implementation of such a device by eliminating the need for a PhC composed entirely of fabrication-sensitive bowties.

1.5 Simulation techniques

While the behavior of light propagating in simple infinitely-long, one-dimensional photonic crystals can be calculated quite well using an analytical approach based in Maxwell's Equations, the propagation of light in more complicated structures with higher dimensionality is far less well-behaved, and this renders impossible a simple analytical approach. Thus, numerical methods for predicting the optical response of photonic structures become necessary to accurately calculate solutions to Maxwell's equations for practical photonic crystals.

1.5.1 The finite-difference time-domain method

Among the suite of simulation and modeling tools available to a photonic crystal designer, the finite-difference time-domain (FDTD) method is among the most powerful. FDTD simulations provide a brute-force means to simulate the propagation of light through optical structures. The simulation space is discretized into a grid of cells, and Maxwell's equations are solved for each

cell at discrete steps in time [19,20]. Because the algorithm operates in the time domain, this method makes it possible to calculate the transient optical response of a desired structure and to even watch the progression of the electromagnetic field in the simulated timeframe.

Since the FDTD method is a time-domain approach, a caveat is that the computational resources required scale with the time simulated. Likewise, large simulation spaces or fine spatial discretization consume more resources, requiring large amount of memory. The resolution of the spatial discretization is a matter of the "meshing" being utilized, where the simulation time in a 3D simulation scales with the mesh size, dx, as $1/dx^4$. This places practical limitations on what can be easily simulated, especially in cases of very large optical structures or highly resonant structures (i.e., those with long photon lifetimes). Certain techniques exist to deal with these computational limits, such as utilizing natural symmetries in the simulation to reduce the spatial volume that needs to be simulated. Also, rather than meshing a uniform Cartesian grid, the meshing can be varied throughout the simulation space to better conform to the structure being modeled and avoid wasting resources meshing specific regions more finely than necessary. Some of these techniques are discussed in Section 3.2.4. In the work described in the following chapters, Ansys Lumerical [21] and MIT's Meep [22] software packages were used for FDTD simulations. With the appropriate simulation configuration, an FDTD solver is capable of accurately predicting the flow of light in periodic structures, and the Q and V_m of designed PhC nanobeams can be computed and tailored in this way.

1.5.2 Eigenmode analysis

In dealing with waveguide-based components for photonic integrated circuits, it often becomes necessary to study the optical characteristics of the guided modes for a particular

waveguide structure. The Lumerical DEVICE Suite includes a finite-difference eigenmode (FDE) solver that can assist in this task. Similar to the FDTD algorithm mentioned above, the FDE solver discretizes the spatial profile of the simulated structure; however, instead of solving Maxwell's equations at proceeding timesteps, this method computes a solution to Maxwell's equations as a matrix eigenvalue problem for the discretized space. This allows the user to extract information about the eigenmode, including the spatial profile of the mode, the effective index, and the loss. Many situations in photonic design require knowledge of the mode profile for waveguides, the extent of the evanescent field outside the structure, or the number of modes supported by a particular waveguide geometry. The FDE technique is, thus, a powerful tool for designing and optimizing waveguide-based photonic structures.

1.5.3 Band calculation

The utility of photonic crystals comes from their unique photonic band structures and the existence of a band gap of disallowed frequencies. The ability to examine and craft the band structure of a given PhC structure is important for tailoring the optical response of the PhC for use in practical devices. Since analytical calculations fail for more advanced, finite PhC geometries, calculating the band structure becomes a matter of numerical computation, and one such tool for this is MIT Photonic Bands (MPB). To arrive at the band structure for a given PhC, MPB computes definite-frequency eigenstates of Maxwell's equations in a 3D discretized space. This is a frequency domain technique, as opposed to FDTD, and is well-suited to quickly calculating the dispersion relations and eigenstates for periodic dielectric structures.

Another strategy for calculating PhC band structures is to simulate the unit cell in FDTD, for example Lumerical FDTD, and extract each frequency where a band exists across a range of

wave vectors. This is done by using Bloch boundary conditions and simulating a "cloud" of randomly-oriented dipoles scattered throughout the simulation space to excite as many modes as possible. The wave vector, k, being simulated is determined by the Bloch boundary conditions, so multiple simulations must be run to sweep across each k in the band structure. In each simulation, the resonant frequencies that persist while other frequencies decay show the location of bands. While this technique is less direct, and in many cases slower, it does allow for more advanced meshing and boundary condition options to be used in Lumerical's software package.

1.6 Overview of dissertation

Throughout this dissertation, I will endeavor to detail the fundamental principles of photonic crystal theory for light-matter interaction and demonstrate the application of novel design methodologies for PhCs in the realm of optical signal processing. It is intended that the work described herein highlights the potential of PhC cavities to find use in emergent technologies, as well as demonstrate areas where integrated photonics as a field is applicable toward solving real-world problems in information processing and communications in the near future.

In the first two chapters, novel design techniques for these integrated PhC cavities are studied. Chapter 2 deals with the use of a side-coupled bus waveguide to realize high-transmission, high-quality-factor resonances and, in addition, proposes a novel uniform-mirror PhC design enabled by the use of side-coupling. In Chapter 3, a methodology for combining different unit cell geometries into a single PhC cavity is demonstrated, alongside thorough discussion of simulation and optimization strategies for achieving this. In Chapter 4, a hybrid Si-VO_2 PhC cavity platform for optical modulation is proposed, using a phase-change material to modulate the optical properties of a PhC nanobeam. In Chapter 5, a PhC nanobeam cavity with bowtie unit cells is

investigated for all-optical switching by relying on the high peak energy density enabled by the bowtie shape. Finally, Chapter 6 presents a summary of the key results of this dissertation and discusses the broader impact of the work within the fields of integrated photonics and, more generally, photonic information processing.

CHAPTER 2

High-transmission intensity using side-coupling waveguides

S. I. Halimi, S. Hu, F. O. Afzal, and S. M. Weiss, "Realizing high transmission intensity in photonic crystal nanobeams using a side-coupling waveguide," *Opt. Lett.* **43**, 4260-4263 (2018).

2.1 Introduction

Photonic crystal nanobeam cavities are relatively compact, one-dimensional, on-chip PhCs that are capable of simultaneously achieving high quality (Q)-factors and small mode volumes. Conceptually similar to Fabry-Pérot cavities comprising two Bragg mirrors surrounding an optical cavity, the design of the highest-Q PhC nanobeams requires that the electromagnetic fields are allowed to follow a Gaussian-like decay profile to prevent significant scattering losses that would otherwise result at the cavity–mirror interfaces [11,23]. The deterministic design method for PhC nanobeams [10,18] provides a step-by-step approach to achieve this desired field profile and form high-Q PhC nanobeams in a variety of material systems [24,25]. The filling fraction of the PhC unit cell determines the so-called mirror strength of that unit cell [3]. By linearly changing the mirror strength between the outer maximum mirror strength unit cells and the central cavity, a Gaussian field profile can be obtained. The straightforward design method and versatility in the choice of material system, combined with fabrication requirements that are now achievable in high-throughput foundries [26], make PhC nanobeams appealing for a wide range of applications, including sensing [26], nonlinear optics [27], optomechanics [28], optical trapping [29], and quantum information processing [7]. The addition of slots [16,17], or subwavelength dielectric features such as bow-ties [13,30], can be used to further reduce the mode volume and increase the

peak energy density while maintaining a high Q, thus opening the door to improved performance metrics in many of the aforementioned applications.

The traditional approach to couple light into a PhC nanobeam cavity is using an in-line configuration in which light from a contiguous input waveguide passes through the array of holes comprising the PhC nanobeam before being detected on the opposite side of the nanobeam from a contiguous output waveguide. In this scheme, there exists a trade-off between Q and transmission intensity. More mirror unit cells or higher mirror strength unit cells are required for stronger confinement of light in the cavity and higher Q, but as light from the feeding waveguide interacts with these mirrors, Bragg reflection causes a commensurate decrease in transmission intensity. While the deterministic design method has been reported in simulation to achieve PhC nanobeams with ultrahigh Q ($>10^7$) and ultrahigh on-resonance transmission (>95%) [11], and there is at least one prior experimental demonstration of a PhC nanobeam with $Q > 10^4$ and transmission >70% [19], in practice, realizing high transmission intensities for the fundamental mode of high-Q PhC nanobeams is challenging. Some groups utilize a resonant scattering technique [12] or detect the vertical radiation spectrum [17] to measure higher extinction ratio resonances that more closely represent the intrinsic Q of the PhC nanobeam cavity. However, for practical application in most on-chip applications, these techniques cannot be utilized. Other groups have reported using a side-coupled PhC nanobeam configuration to measure resonances by directly coupling into and out of the central cavity region of the nanobeam, avoiding transmission through the high mirror strength regions [31–35]. We note that in the side-coupling scheme, because light that is not resonant in the PhC nanobeam is transmitted through the side-coupler, the transmission spectrum is characterized by a high-intensity baseline and resonance dips. In contrast, the transmission spectrum of a PhC nanobeam in the in-line configuration is characterized by a low-intensity

baseline and resonance peaks. Here, we show through direct experimental comparison that in cases in which the reflectivity of the PhC nanobeam mirror segments precludes a transmission measurement of the fundamental resonance using the in-line configuration, the fundamental resonance of the same PhC nanobeam can be measured when a side-coupled waveguide is utilized. Moreover, we demonstrate a simplified design approach that can be used for side-coupled PhC nanobeams. Finite-difference time-domain (FDTD) simulations reveal that, in certain cases, the tapered radius Gaussian mirror unit cells specified by the deterministic design method may be replaced by uniform mirror unit cells with the same radius.

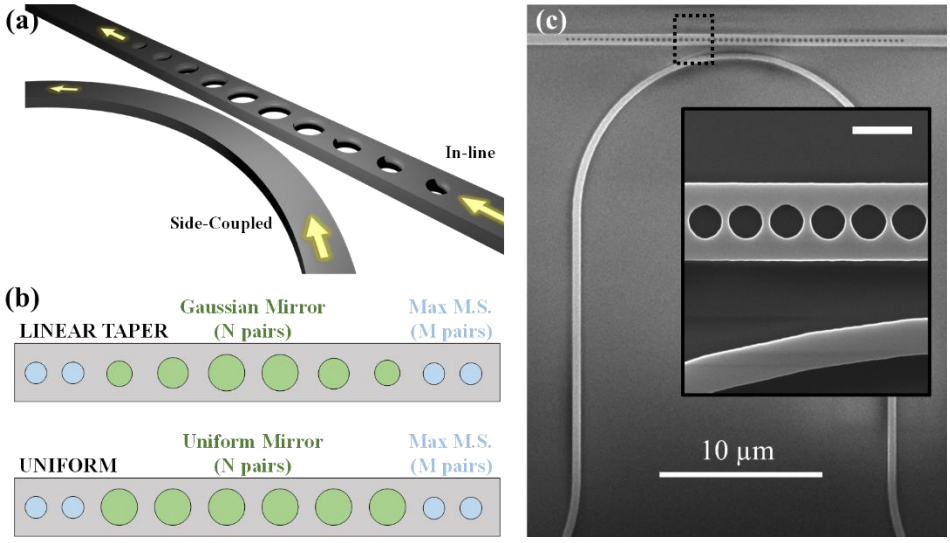

Figure 2.1. (a) Schematic illustration of the PhC nanobeam with a side-coupling waveguide. (b) Nomenclature used to describe the nanobeam mirrors, with either Gaussian or uniform mirrors surrounded by maximum mirror strength (M.S.) mirror segments. (c) SEM image of PhC nanobeam with side-coupler. Inset: magnified view of the boxed region (scale bar = 500 nm).

2.2 Study of side-coupling waveguide

2.2.2 Design and simulation

Figure 2.1(a) shows a schematic illustration of the PhC nanobeam design investigated in this work, which supports both in-line and side-coupled transmission measurements. The side-coupling waveguide is adjacent to the PhC nanobeam and bends toward the center of the nanobeam cavity to enable evanescent coupling of light from the side-coupling waveguide into the nanobeam cavity. While the incident light must traverse the entire PhC nanobeam, including all of the mirror segments, before a transmission measurement can be made using the in-line configuration, in the side-coupled configuration, the transmission intensity does not suffer with increased mirror strength, since light is coupled directly into and out of the central cavity region of the nanobeam. We note that the presence of the side-coupled waveguide does slightly reduce the loaded Q of the PhC nanobeam cavity when measured using the in-line configuration. The PhC nanobeam cavity is designed to operate with a TE-polarized, dielectric-mode resonance within the desired wavelength range, i.e., with the modal energy density concentrated in the silicon. The following parameters were used for the silicon nanobeam design investigated through both simulation and experiment in this work. The nanobeam width and thickness were 700 nm and 220 nm, respectively, and the lattice constant of the holes was 350 nm. A cavity length of zero was specified, and two distinct regions of mirrors were included on both sides of the cavity: N mirror pairs of tapering filling fraction that form the Gaussian mirrors and M mirror pairs of maximum mirror strength placed at the ends of the PhC to limit energy loss through the in-line coupled input and output waveguides. Figure 2.1(b) delineates the nomenclature used in this work to describe the different mirror regions. Referring to the upper part of Fig. 2.1(b) for our initial work, 15 Gaussian mirror pairs (N = 15) were chosen. The holes comprising the Gaussian mirror were varied in radius from

135 nm at the center of the PhC to 100 nm, with the filling fraction tapering quadratically to achieve a linearly varying mirror strength. The relationship between mirror strength and filling fraction of the holes, obtained using three-dimensional band diagram simulations, is shown in the inset of Fig. 2.2. Different numbers of mirror pairs of maximum mirror strength (M = 0, 5, 10), with radii of 100 nm, were added at the ends of the nanobeam to investigate their effect on the transmission intensity of the nanobeam resonances.

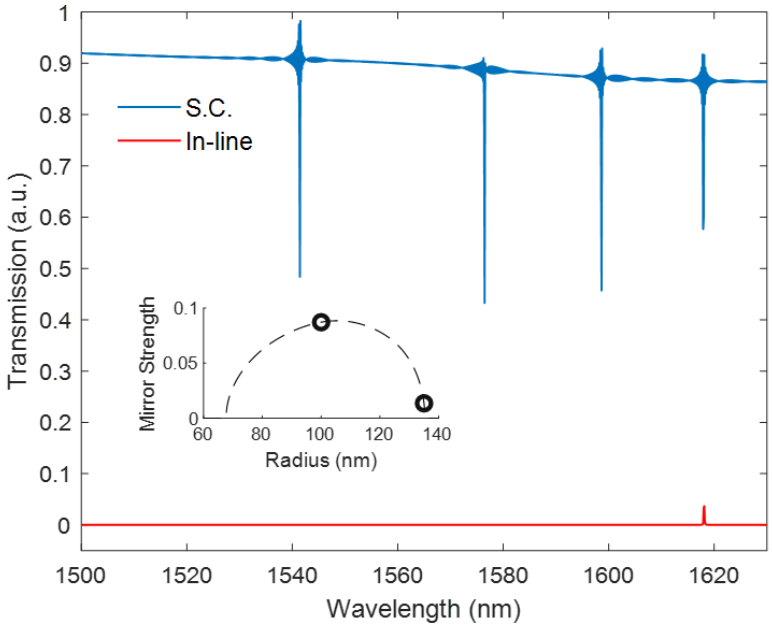

Figure 2.2. Simulated transmission spectra of a PhC nanobeam (N = 15, M = 10) for light coupled through the feeding waveguide (i.e., in-line) or through a side-coupling (S.C.) waveguide. Inset: simulated mirror strength of PhC unit cells with different hole radii.

Three-dimensional FDTD simulations were carried out to compare the calculated transmission of the same PhC nanobeam when coupled using in-line and side-coupling configurations. In order to conserve computational resources, the simulation assumed a suspended

PhC nanobeam and a truncated side-coupling waveguide curved as a half ellipse with a radius of 4 μm in the direction along the length of the nanobeam and 2.4 μm in the perpendicular direction. There were N = 15 Gaussian mirror pairs and M = 10 maximum mirror strength mirror pairs. At the closest point, the coupling gap between the side-coupler and the nanobeam was 300 nm. The transmission spectrum was simulated initially with a broadband source exciting a waveguide mode in the in-line feeding waveguide and subsequently with a waveguide mode in the side-coupler. Figure 2.2 illustrates the advantages of the side-coupled PhC nanobeam design. While the transmission intensity through the in-line coupled PhC nanobeam is nearly zero across the entire simulated bandwidth, with the exception of one low-contrast resonance near 1618 nm, the side-coupled PhC nanobeam supports four high-contrast transmission resonances and high transmission intensity across the simulated bandwidth. The transmission intensities of the three lowest order modes of the in-line PhC nanobeam are calculated to be less than 0.3% based on additional FDTD simulations that consider radiative losses [19], and such low intensities are not likely measurable in experiment. The loaded Q of the fundamental resonance in the side-coupled configuration is 6.5×10^4. We note that the resonance corresponding to the fourth-order mode occurs at the same wavelength for both coupling configurations; by using the same geometric layout in simulation and changing only the source location, we ensure that the effective index of each mode supported in the PhC nanobeam cavity is the same for both coupling schemes. We further note that the high-frequency oscillations in the transmission spectrum of the side-coupled PhC nanobeam are artifacts of the finite duration of the simulation (simulation time = 40 ps).

2.2.3 Experimental verification

Several PhC nanobeam cavities were fabricated to verify the transmission characteristics predicted in simulation. The aforementioned PhC nanobeam designs (N = 15; M = 0, 5, 10) were patterned on a silicon-on-insulator wafer with a 220 nm silicon device layer and 3 μm buried-oxide layer (Soitec) using standard electron beam lithography (EBL) and reactive ion etching (RIE) protocols, similar to what we have previously reported [36]. Chips were cleaved from the wafer and sized appropriately to accommodate multiple instances of the device pattern (created as a GDSII file), and each was spin-coated with a 300-nm thick layer of the electron beam resist ZEP520A at 6000 rpm for 45 seconds and received a 2-minute pre-bake at 180º on a hot plate. The patterns were then written into the resist with a JEOL9300FS EBL system at an acceleration voltage of 100 kV with doses defined for each layer in the pattern at permutations of a base dose of 300 μC/cm^2. The exposed patterns were developed in a bath of xylenes for 30 seconds, rinsed with isopropyl alcohol, and etched to transfer the pattern into the silicon device layer. The RIE process was performed in an Oxford PlasmaLab 100, etching for 2 minutes in a chamber of C_4F_8/SF_6/Ar gas to remove the un-masked silicon, and a final 10-minute descum removed the remaining resist from the chips to leave the final silicon device.

The side-coupling waveguide was patterned to extend along the length of the chip parallel to the feeding waveguide, curving in the center toward the nanobeam with a radius of 10 μm. The coupling gap was 320 nm at the closest point. A scanning electron microscope (SEM) image of one of the fabricated structures is shown in Fig. 2.1(c). Transmission measurements were carried out by coupling transverse electric (TE)-polarized light from a tunable laser source (Santec TSL-510) into the in-line or side-coupled input waveguide using a tapered fiber (OZ Optics). A second

tapered fiber collected light from the in-line or side-coupled output waveguide, and a fiber-coupled optical power meter (Newport 2936-C) was used to detect the output signal.

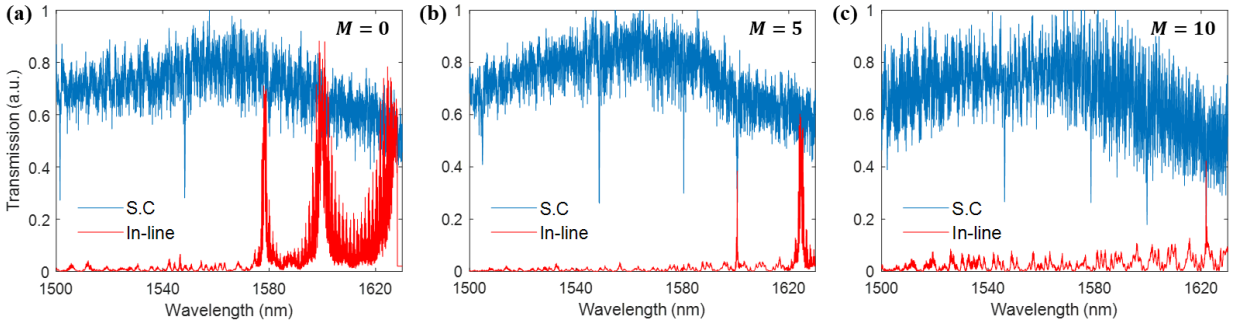

Figure 2.3. Transmission spectra for a nanobeam with N = 15 Gaussian taper mirror segment pairs, coupled in-line and using the side-coupling waveguide. Increasing the number of maximum mirror strength mirror pairs at the ends of the Gaussian mirrors from M = 0 in (a) to M = 5 in (b) and M = 10 in (c) decreases the transmission intensity in the in-line case, such that it is indistinguishable from noise, whereas excitation of the modes using the side-coupler is not affected by increased mirror strength.

Figure 2.3 shows the experimentally measured transmission spectra for the three different PhC nanobeam cavity designs using both in-line coupling and side-coupling configurations. The laser input power was kept constant for all of the measurements shown so that the transmission intensities in each spectrum could be compared. In the traditional in-line coupling scheme, the Q increases with the addition of maximum mirror strength mirror segments at the ends of the PhC due to stronger confinement of light between the mirrors and less energy dissipating out of the cavity. However, the transmission intensity also decreases until resonances are indistinguishable from noise with M = 10.

The behavior of the in-line coupled PhC nanobeam cavities is compared with the transmission spectra of the same structures when light passes through the side-coupling waveguide. As shown in Fig. 2.3, while the peak heights decrease with increasing mirror strength for in-line

measurements, the transmission remains nearly the same in the side-coupled case. For the nanobeam with the largest mirror strength [M = 10, Fig. 2.3(c)] whose resonance peaks are below the noise floor when measured in-line, the peaks are accessible when measured with the side-coupler. Moreover, lower-order modes can be resolved in a side-coupled nanobeam regardless of how many maximum mirror strength unit cells are present. We observed good agreement between the loaded Q measured in experiment (1.3×10^4) and calculated in simulation for the fundamental mode. A side-coupler design that incorporates better mode matching between the side-coupled waveguide and PhC nanobeam cavity could lead to higher contrast transmission resonances [37].

2.3 Novel PhC nanobeam design

2.3.1 Nanobeam with uniform mirrors

The use of the side-coupler opens up the possibility to explore PhC nanobeam designs with alternate, non-tapered mirror configurations. While the linear taper in filling fraction of the mirror pairs is a practical necessity for light to penetrate into the PhC cavity through the mirrors (i.e., in-line coupling), bypassing the mirrors and coupling light directly into the cavity via a side-coupler removes the requirement to use a tapered mirror region. The lower portion of Fig. 2.1(b) shows a proposed PhC nanobeam cavity design comprising mirror segments of uniform filling fraction surrounded by maximum mirror strength pairs. Such a PhC cavity could be utilized only with a side-coupler or other direct cavity coupling approach (e.g., out-of-plane evanescent coupling with tapered fiber [38]). Three-dimensional FDTD simulations were performed to compare the intrinsic Q of PhC nanobeam cavities on SiO_2 substrates with either Gaussian or uniform mirrors (N = 5–35) surrounded by M = 10 maximum mirror strength mirror pairs, as shown in Fig. 2.4(a). Interestingly, the Q of the side-coupled PhC nanobeam with Gaussian mirrors is only slightly

higher than that of the side-coupled PhC nanobeam with uniform mirrors. Consequently, given the additional complexity in process development and fabrication required to achieve the precise dimensions of the unit cells constituting the Gaussian mirror, in many cases, it may be preferable to design and fabricate side-coupled PhC nanobeams with uniform mirrors, as these PhCs require only two different unit cell building blocks. We believe the slightly lower Q associated with incorporation of the uniform mirror is due in large part to scattering at the interface between the uniform mirror and maximum mirror strength unit cells. The electric field distribution for a side-coupled PhC nanobeam with N = 35 uniform mirror pairs [Fig. 2.4(b)] shows that the electric field does not decay completely before reaching the maximum mirror strength mirror pairs and does not achieve a Gaussian field profile. The electric field distribution for a side-coupled PhC nanobeam with N =35 Gaussian mirror pairs is shown in Fig. 2.4(c) for comparison; the Gaussian field profile in this case is evident. We note that although the Q of side-coupled PhC nanobeam cavities with Gaussian and uniform mirrors is similar, the different electric field distributions should be considered when determining which design is more suitable for the desired application.

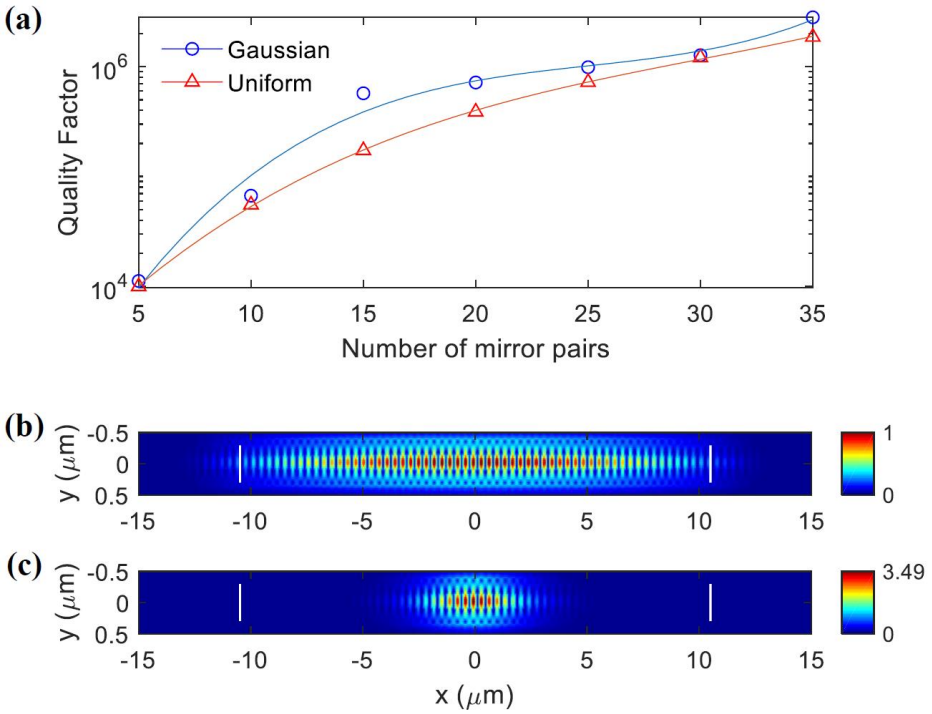

Figure 2.4. (a) Comparison of Q for fundamental resonance of PhC nanobeams with Gaussian versus uniform mirrors as the number of mirror pairs, N, increases. Solid lines are added to guide the eye. (b), (c) Electric field profiles for fundamental resonance of N = 35 nanobeam with (b) uniform mirrors and (c) Gaussian mirrors. White lines indicate where the maximum mirror strength regions begin.

2.3.2 Dependence of resonant wavelength on the PhC taper length

Varying the number of mirror pairs in simulated studies of the PhC nanobeam also reveals another key trend in addition to that seen previously in the calculated quality factor. Figure 2.5 shows the resonant wavelength that was recorded for each PhC nanobeam design. For the Gaussian mirror design, we can observe that the wavelength varies quite dramatically with the length of the PhC nanobeam, decreasing (i.e., a blue-shift) with the inclusion of more unit cells. As the PhC length increases, the wavelength begins to converge to a steady value. This behavior is consistent with the theory of how light is confined in the structure across the spectrum. The resonant wavelength, as determined by the central unit cell at the cavity region, would be calculated via deterministic design [11] by assuming periodic boundary conditions to simulate an infinitely long

one-dimensional PhC and by predicting the wavelength to be located near the band edge of the infinite Bloch structure. The final mirror in the tapering mirror region is chosen to produce high mirror strength for this wavelength. However, due to the finite length of the practical device, the resonant wavelength cannot equal that arrived at by considering an ideal, infinite PhC. For a dielectric mode resonance in a short PhC nanobeam cavity, the wavelength is red-shifted to longer wavelengths due to higher effective index of the resonant mode realized by the short taper. With the addition of more unit cells, the design will more closely resemble (though never quite meet) the infinite case, and therefore the actual wavelength will more closely match the ideal wavelength, resulting in the blueshift seen in Fig. 2.5. However, in the uniform mirror design, this consideration no longer applies because there is not a taper to significantly shift the effective band edge. Thus, for a sufficiently long uniform mirror PhC nanobeam, the resonant wavelength does not have a strong dependence on the device length. For very short uniform mirror nanobeams of fewer than 10 mirror pairs, the PhC may not be long for enough the formation of a proper Bloch wave occurring at the intended band edge. These results highlight an important insight that the length of the PhC nanobeam taper is an essential consideration for the Gaussian mirror design when trying to achieve a resonance at a desired wavelength, but the length may be less important when using the uniform mirror design approach with side-coupling. Note also that the uniform mirror design case has a lower resonance wavelength than the Gaussian mirror design. This can be attributed to the fact that the larger radius air holes from the center of the cavity are spread across the length of the uniform mirror design, producing a lower effective index, in addition to the greater similarity of the uniform design to the ideal PhC that is an infinite sequence of that same unit cell.

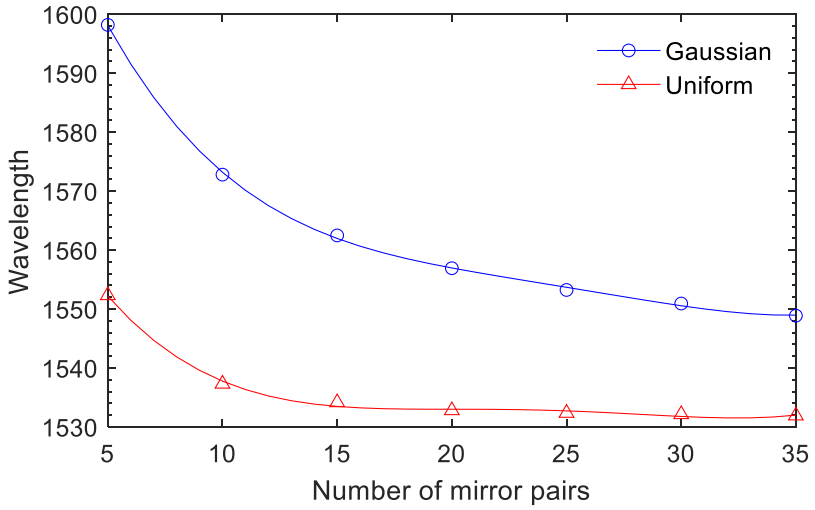

Figure 2.5. Resonant wavelength of the fundamental resonance for PhC nanobeams simulated by FDTD with Gaussian (blue) and uniform (red) mirrors as the number of mirror pairs increases from N = 5 to N = 35.

2.4 Summary

In summary, we have demonstrated a PhC nanobeam cavity with a side-coupling waveguide capable of achieving high-Q resonant modes without suffering from the usual trade-off between Q and transmission intensity that is exhibited by in-line coupled PhC nanobeam cavities. For a particular PhC nanobeam cavity design with a large number of high mirror strength unit cells, we show in experiment that while in-line coupling leads to complete suppression of low-order modes in transmission, side-coupling of the same PhC nanobeam enables measurement of those resonances. The improvement in transmission characteristics afforded by the side-coupling waveguide does come at a slight penalty in device footprint, although the configuration importantly maintains compatibility with on-chip operation for a variety of multiplexed applications spanning biosensors to quantum information processing. FDTD simulations further suggest that side-coupled PhC nanobeam cavities can be designed with only two unit cell building blocks— maximum mirror strength unit cells on the outside and minimum mirror strength unit

cells on the inside—while maintaining Q-factors comparable to more sophisticated, deterministically designed PhC nanobeam cavities.

CHAPTER 3

Controlling PhC mode profiles with mix-and-match unit cells

S. I. Halimi, Z. Fu, F. O. Afzal, J. A. Allen, S. Hu, and S. M. Weiss, "Controlling the mode profile of photonic crystal nanobeam cavities with mix-and-match unit cells," *J. Opt. Soc. Am. B* **37**, 3401-3406 (2020).

3.1 Introduction

For many applications in photonics, having a high degree of light-matter interaction is essential. In some of these applications, having a low-loss resonance is important, the metric for which is the quality factor (Q), while other applications rely on having high peak energy density and low modal volume (V_m). Photonic crystal cavities have been demonstrated in a wide range of on-chip applications for light-matter interaction, including optical modulators [39,40], lasers [41,42], and optical biosensors [43,44]. While the Q of PhCs can be tuned over a large range ($Q \sim 10^2 - 10^6$) in a straightforward manner by changing the number of unit cells and the dimensions thereof, it remains difficult to manipulate the mode distribution and energy density across the unit cells. Ultimate control of the performance of resonant PhC devices requires tuning both Q and V_m independently, as some applications are impaired by too high a Q (e.g., ultrafast switching). In these cases, ultralow V_m and modest Q may be ideal. Recent work has demonstrated it is possible to leverage subwavelength design for subwavelength mode concentration in PhC cavities [14,15,27]. The antislot and bowtie unit cells redistribute light within the unit cell to critical dimensions near 50 nm and 10 nm, respectively [14,15]. However, these designs localize the field to very small regions across all unit cells. For applications leveraging optical nonlinearities or single photon emitters, for example, it may not be desirable for multiple unit cells

near the central cavity unit cell to support extremely high light intensity. Consequently, another design approach that allows control over the mode distribution across all unit cells of PhC is needed. Furthermore, PhC cavities with subwavelength features in all unit cells [e.g., Fig. 3.1(a)] are difficult to fabricate at scale with high fidelity, as minor fluctuations in process conditions can greatly impact the uniformity of features near the lithographic limit, with this effect being more pronounced the more of these small features are present. It is, thus, advantageous to use the minimum number of subwavelength features necessary to achieve the desired mode confinement alongside more fabrication-tolerant traditional PhC unit cells. For example, at the foundry level, fabrication of one bowtie unit cell would allow more control over the uniformity and could be more easily realized than a series of twenty or more bowtie unit cells in a single PhC device. This general approach of considering inclusion of PhC unit cells of different shapes has been followed in 1D PhCs with an air slot in the center of the cavity [18] and has been recently proposed [45,46] and experimentally reported [45] with a 1D PhC possessing a single bowtie unit cell in the center of the cavity. However, fundamental design rules to realize optimal performance metrics in such mixed unit cell PhCs have not been established. Here, we report a design methodology that can mix and match fabrication-tolerant unit cells with a subwavelength-critical unit cell, harnessing the positive attributes of subwavelength mode concentration while greatly improving the ease of fabrication and achieving much broader control of the mode distribution across all PhC unit cells.

In the conventional PhC design approach, all unit cells in a PhC have the same shape (e.g., circles, rectangles); cavities are formed by tapering the PhC unit cells between highly mirroring regions and the cavity region to ensure a smooth transition and minimize abrupt changes between unit cells (e.g., by gradually changing the unit cell radius, lattice spacing, or nanobeam width), enabling a Gaussian field profile with low scattering losses [11,19]. Figure 3.1(a) shows an

illustration of a bowtie PhC cavity designed in this traditional way with one unit cell geometry (i.e., the bowtie) being tapered in size across the nanobeam. In the mix-and-match unit cell design approach introduced in this work, we demonstrate that it is possible to add a single unit cell with a subwavelength-sized critical feature to an otherwise traditionally designed PhC nanobeam without incurring significant scattering losses if appropriate care is taken in selecting the unit cell radius and width. While this work introduces an approach for designing mixed unit cell PhCs by using two distinct unit cell geometries, we believe it is possible to incorporate additional unit cell geometries at different locations in the PhC through a similar design procedure, allowing fine manipulation of the mode distribution and some control over the local phase and amplitude of light within the PhC. Therefore, the design freedom afforded by mixing and matching unit cells could facilitate, for example, spatially multiplexed biosensing, directional light emission, and other new avenues for PhC functionality.

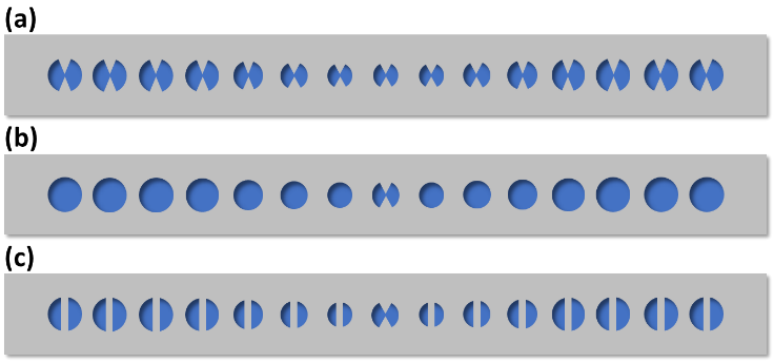

Figure 3.1. Schematic illustration of (a) 1D PhC composed of bowtie unit cells, (b) mix-and-match PhC with a single bowtie unit cell at the center of the cavity, surrounded by circular air hole unit cells forming the mirrors, and (c) mix-and-match PhC with bowtie cavity unit cell and antislot mirror unit cells.

3.2 Design and optimization

3.2.1 Design approach

The design process for the "mix-and-match" method consists of two primary steps: a "mix" step and a "match" step. In the mix step, the shape of the default unit cells is first determined. Default unit cells are typically chosen to have large, easy-to-fabricate features such as circles or rectangles. Second, the geometries of the functional unit cells are identified. Functional unit cells are chosen to have unique shapes for specialized purposes, such as subwavelength mode concentration, opto-mechanics, or polarization control. The "match" step follows an empirical optimization approach to simultaneously reduce mismatch between the band structures of both types of unit cells in k-space and between their spatial mode profiles [47,48]. This matching process can be accomplished in simulation through multi-dimensional parameter sweeps, which typically require at least two tuning parameters to be able to effectively meet the matching condition and reduce scattering losses. Here, we first adopt a brute-force simulation approach to allow full insight on the effect of different physical parameters on the optical properties of the mixed unit cell PhC to be revealed. In general, other optimization strategies may be desirable depending on the nature of the functional unit cell parameters being tuned and how much is known *a priori* about the topology of the parameter space being explored (e.g., approximate maximum location from theory or the existence of local maxima). Accordingly, after gaining knowledge of the topology of the parameter space explored for the mixed unit cell PhCs, we subsequently demonstrate that a gradient optimization approach can be used to find near-optimal design solutions in a computationally efficient manner.

To facilitate maximum control over functional unit cells with subwavelength features, an air-mode PhC, whose resonance of interest is near the air band edge, is utilized for demonstrating

the mix-and-match approach. Air-mode PhCs localize light within the low-index air hole region of the unit cells [10], and electromagnetic boundary conditions can then be exploited to dictate how modal energy is distributed within the unit cell [14]. In this way, subwavelength features can be introduced in the air holes to provide a greater degree of control over the modal distribution in those unit cells. For example, a subwavelength feature such as a bowtie can further localize and confine light within a PhC, establishing two levels of optical confinement in which the air-mode design concentrates modal energy in the air holes of the lattice and then the dielectric bowtie inside the air hole effectively "funnels" the light to the tips of the bowtie. Similarly, an antislot unit cell can localize modal energy inside a high-index, vertical dielectric bar spanning an air hole, based on an interface effect that functions as the opposite of the slot effect [14,16]. Operationally, when utilizing the fundamental resonance of an air-mode PhC cavity, the central cavity unit cell is the most impactful unit cell to substitute with a functional unit cell. It is also the most straightforward to change to a functional unit cell using the mix-and-match approach.

3.2.2 Numerical results

To demonstrate the mix-and-match design technique, we designed two mixed unit cell PhC nanobeams having a bowtie-shaped functional unit cell as the central cavity unit cell, one with circular air holes as the default PhC unit cells and the other with antislots as the default unit cells, as shown in Fig. 3.1(b-c). We note that other unit cell shapes could have been utilized without a loss of generality in the mix-and-match design approach. Three-dimensional finite-difference time-domain (FDTD) simulations (Lumerical Inc.) were first carried out to design circular air hole and antislot PhC nanobeams composed of unit cells of uniform shape, following established deterministic design procedures [11]. Band edge calculations were done to determine the desired

radii of the central cavity unit cell and maximum mirror strength segments for each PhC nanobeam. The number of mirror segments between the central cavity unit cell and unit cells with maximum mirror strength (i.e., the taper length) was chosen to produce a fundamental resonance with $Q \geq 10^4$ at an appropriate near-infrared, telecom-band wavelength with sufficiently high transmission through the nanobeam to be easily measurable in experiment [49]. The resulting simulated circular air hole PhC cavity had a nanobeam width of 700 nm and period of 400 nm with 9 tapering mirror segment pairs ranging from 93 – 135 nm in radius and 5 maximum mirror strength unit cells at each end. The fundamental air-mode resonance of the circular air hole PhC cavity has a simulated $Q = 7.9\times10^4$ and $V_m = 1.5\times10^{-2}\ (\lambda/n_{air})^3$ at 1520 nm. The antislot PhC cavity was designed with a nanobeam width of 700 nm, period of 450 nm, 15 mirror pairs with radius 160 – 181 nm, and 5 maximum mirror strength unit cells. The dielectric bridges of the antislot segments were designed to be 50 nm wide. We note that introducing an antislot into the air hole of the unit cell lowers the index contrast between that air hole and the adjacent dielectric region, consequently shrinking the size of the band gap; accordingly, we increased the period of the antislot PhC to counteract this effect. The fundamental resonance of the antislot PhC cavity has a simulated $Q = 9.4\times10^4$ and $V_m = 2.8\times10^{-2}\ (\lambda/n_{air})^3$ at 1549 nm. Following this initial optimization, a single bowtie unit cell was inserted into each of the uniform PhC cavity designs, replacing the default unit cell at the center of the cavity with the goal of reducing the cavity mode volume while maintaining a similar Q. The bowtie radius and bowtie unit cell width were varied in a parameter sweep in 3D-FDTD simulations while keeping all other dimensions the same to evaluate the resulting effect on the mixed unit cell Q and V_m. We note that changing these parameters of the bowtie unit cell do not strongly influence mode volume since the energy redistribution due to the bowtie is not a resonant effect; while the bowtie angle and gap size may affect V_m, we do not sweep those parameters here.

We further note that while the radius and width of the functional unit cell are the parameters varied in the “match” step in this work, the desired application of the mixed unit cell PhC should dictate the selected shape of the functional unit cell, and dimensions of the PhC that are most impactful to the desired application should be varied.

For both mixed unit cell PhC designs, a coarse sweep over a wide range of parameters (4 nm step size in radius and unit cell width values) was performed to find the region in parameter space with maximum Q before refining the sweep to a 1 nm step size to settle on a single optimized bowtie radius and unit cell width for each design. Figure 3.2(a-d) shows the results of the larger step size parameter sweeps, both in calculated Q and resonant wavelength. The optimized designs arrived at from these sweeps were further simulated to characterize the resonant modes. Figure 3.2(e) shows the mode profile of the antislot-bowtie nanobeam, demonstrating the ultrasmall energy confinement at the narrow bridge of the bowtie unit cell. Consideration of the mode volume will be discussed later.

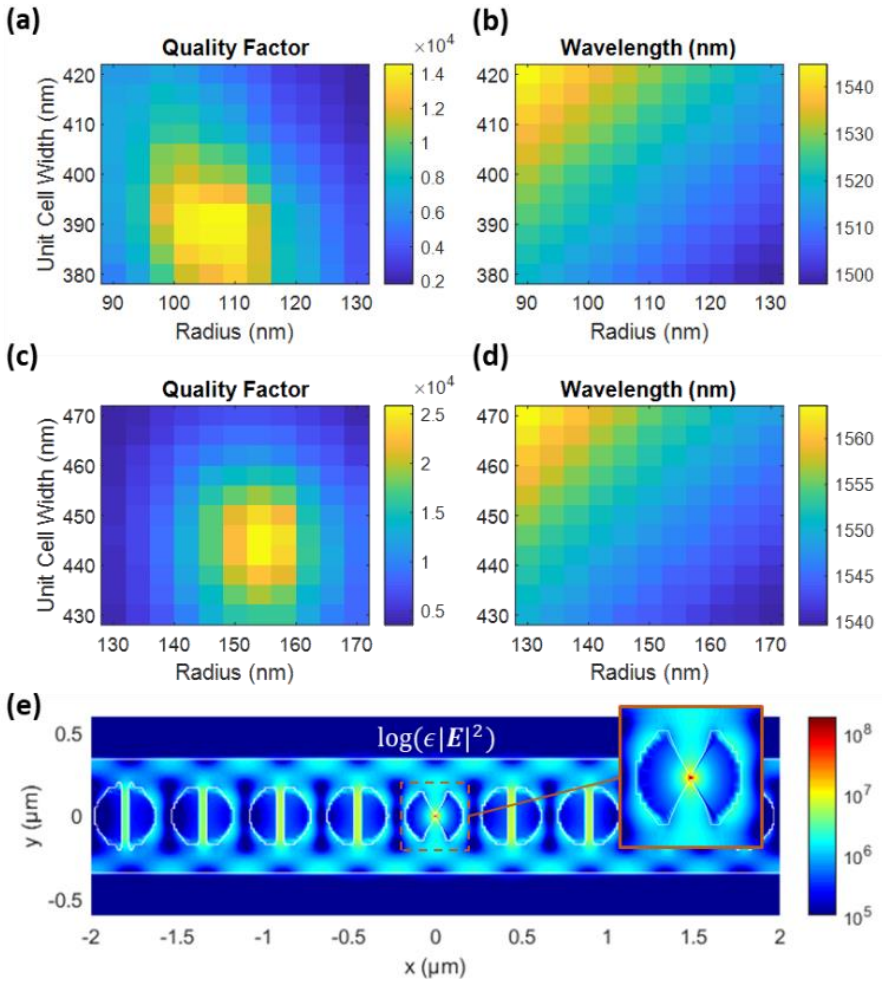

Figure 3.2. Simulated 3D-FDTD parameter sweep of bowtie radius and unit cell width in (a-b) air hole-bowtie and (c-d) antislot-bowtie PhC nanobeams, showing how quality factor and resonant wavelength vary for each combination of parameters. (e) Simulated mode profile of the optimized antislot-bowtie mix-and-match PhC design.

3.2.3 Gradient optimization

This sweep reveals a continuous and smooth dependence of Q on radius and unit cell width along with a single local maximum. This knowledge of the design space topology can be exploited to improve computational efficiency by leveraging appropriate optimization methods that explore a subset of the parameter space while respecting its shape and continuity. Numerical optimization methods such as particle swarm optimization (PSO) and gradient optimization (GO) have been

popular in recent literature for optimizing photonic devices [50–54]. While PSO is effective at avoiding local minima that may exist in a parameter space, it requires many parallel simulations that coarsely span the sample space, generally requiring more computational resources than GO. While GO is less resource-intensive than PSO, it can struggle with parameter spaces that have multiple local extrema found near a global maximum/minimum and spaces with discontinuities in the figure of merit and its gradient. The smoothly varying parameter space with a single, global maximum, seen in the calculated Q results of the parameter sweeps in Fig. 3.2, suggests GO would be a more appropriate choice for optimizing the mixed unit cell PhCs explored here. To verify this hypothesis, we investigated a gradient approach to optimize the bowtie unit cell dimensions with coarse parameter sweep simulation data from Fig. 3.2(a, c). The design optimization paths for both of the previously simulated PhC nanobeam cavities are shown in Fig. 3.3. Figure 3.3(a) shows GO for the air hole-bowtie design starting from an initial choice of bowtie unit cell geometry with the same radius and unit cell width as the central cavity unit cell of the uniform air hole design. It is apparent that this initial guess (circled in red) to maintain radius and unit cell width starts the optimization process at a point in the parameter space located relatively far from the optimal design (circled in blue); however, the GO algorithm was able to arrive at the global maximum in only 5 optimization iterations. Figure 3.3(b) shows GO for the antislot-bowtie design, starting from an initial guess of the cavity dimensions from the uniform antislot design and resulting in only 2 optimization iterations. We believe that fewer optimization iterations were required for the antislot-bowtie PhC because the mode distribution within the antislot unit cell more closely resembles the mode distribution of the bowtie unit cell than does the circular air hole. Each optimization iteration requires three simulations, one to calculate the Q of the simulation point, and two to compute the derivatives of the Q with respect to the radius and unit cell width. These

Q derivatives were approximated by increasing the parameter by a Δ of 5 nm on an interpolated grid of the parameter space and computing ΔQ. This results in a total of 15 simulations needed in Fig. 3.3(a) and 6 simulations needed in Fig. 3.3(b), which are both significantly lower than the 121 simulations used to sample the entire parameter space with a 4 nm grid. Hence, for mixed unit cell designs similar to those studied in this work, a gradient-based optimization strategy should enable functional unit cell parameters to be optimized in a computationally efficient manner.

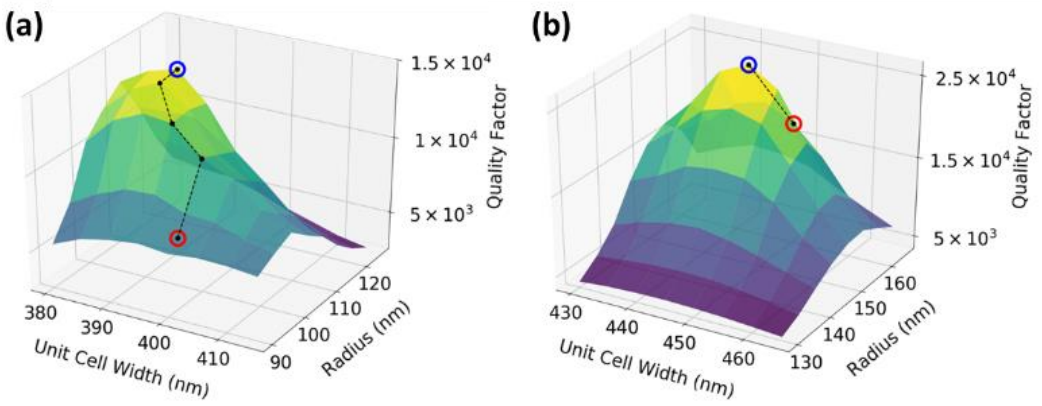

Figure 3.3. Gradient optimization illustrated with the parameter spaces simulated in Fig. 3.2(a, c) starting from bowtie unit cell dimensions of the same radius and unit cell width as the uniform PhC cavity designs. Optimization of calculated Q for (a) the air hole-bowtie PhC nanobeam with initial bowtie radius of 93 nm and unit cell width of 400 nm, requiring 5 iterations, and (b) the antislot-bowtie PhC nanobeam with initial bowtie radius of 160 nm and unit cell width of 450 nm, requiring 2 iterations. The initial point is indicated in red and the converged solution is indicated in blue.

3.2.4 FDTD meshing of subwavelength features

To accurately simulate the mixed unit cell PhCs studied here that incorporate subwavelength features, great care must be given to ensure that the mesh conditions (i.e., the spatial resolution of the simulation) are sufficient to capture those miniscule features. Lumerical FDTD provides a robust interface for controlling the mesh that gets applied to the simulation space.

Specifically, it provides two primary mesh types: uniform and nonuniform meshing. A uniform mesh discretizes the simulation space into a uniform grid of Cartesian cells, the size of which can be specified by the user, whereas the non-uniform mesh is comprised of cells which vary in size according to what is contained within the simulation space. The non-uniform mesh should ideally be coarse for large features and fine for small features, while reducing the computational resources required compared to a uniform mesh.

The antislot and bowtie inclusions within the unit cells present a unique challenge to FDTD simulations for PhCs operating in the near infrared. FDTD, as a technique, is not well-suited to compute Maxwell's equations for situations in which the wavelength of light is much larger than the minimum feature size, and neglecting this fact results in disastrously long simulation times. Thus, uniform meshing is impractical for the mixed unit cell PhCs we have simulated due to the length of the run time; however, using auto non-uniform meshing will not adequately capture the fine features of the antislot or bowtie and will yield inaccurate results, especially in regards to calculating mode volume. To work around these contradictions, the solution found was to use a combination of auto nonuniform meshing and "mesh override" regions.

We utilized an auto non-uniform mesh everywhere we could, specifically for the SiO_2 substrate and free space surrounding the waveguide by defining it as the default mesh setting. Meanwhile, mesh overrides were created to define areas with uniform meshing at size-critical features. The waveguide received a uniform mesh with a resolution of $a/32$ in x and 10 nm in z. The mesh overrides for the antislots had a resolution of 10 nm in x, and for the bowtie it was 10 nm in x, y and 20 nm in z (except when a fine 3-nm mesh was defined at the center of the bowtie shape). Beyond reducing the size of the mesh resolution to account for smaller features, the use of mesh overrides was also crucial for forcing the Lumerical mesh algorithm to correctly simulate

the dimensions of certain features. For example, without specifying the antislot's 10-nm mesh override region to expand to the interface between the antislot dielectric and the air of the hole (i.e., 50-nm wide to match the antislot), the interface becomes blurred during meshing and the dielectric bar may in fact be simulated to be larger or smaller than intended, by fairly large margins with features that small. Likewise, the waveguide mesh override also helped to guarantee the waveguide width. This can be observed, and even measured, by using an index monitor in the FDTD simulation to record the final mesh that actually gets simulated. This step should be taken an essential sanity check of the meshing being used. To ensure that all the simulated results could be compared fairly, similar mesh settings were used across the various simulations reported here. There are also additional considerations in how the use of symmetries in the simulation can distort the size of features in unexpected ways. All of these factors must be taken into account when simulating PhCs with extremely small minimum feature sizes.

3.4 Discussion and analysis

Examining the full parameter space in Fig. 3.2, it can be seen that the Q can change by nearly one order of magnitude and the resonance wavelength can vary by more than 20 nm when the bowtie unit cell width and radius are tuned over a range of 40 nm each. Interestingly, if having the highest possible Q factor is not necessary for a particular application, the results in Fig. 3.2 show that a wide range in resonance wavelengths is achievable for mixed unit cell PhCs by simply tuning the single bowtie unit cell. For the air hole-bowtie design, maximum Q occurs with a bowtie radius of 109 nm and unit cell width of 390 nm. For the antislot-bowtie design, these values are 155 nm and 444 nm, respectively. To properly capture the mode confinement at the ultrasmall "knot" in the center of the bowtie, the Q and V_m values are calculated using FDTD simulations

with non-uniform, 3 nm meshing locally in the region surrounding the knot of the bowtie. The air hole-bowtie PhC has $Q = 1.2\times10^4$ and $V_m = 1.6\times10^{-4}\ (\lambda/n_{air})^3$ at a wavelength of 1515 nm, and the antislot-bowtie PhC has $Q = 2.7\times10^4$ and $V_m = 2.2\times10^{-4}\ (\lambda/n_{air})^3$ at a wavelength of 1549 nm. These simulated values, along with those of the comparably simulated (i.e., with similar meshing) uniform designs discussed earlier, are summarized in Table 3.1. For reference, we also include in Table 3.1 the simulated Q and V_m values for a uniform all-bowtie PhC nanobeam [Fig. 3.1(a)] with the same number of unit cells as the antislot PhC and a taper in radius from 150 nm to 170 nm. The fundamental resonance for this all-bowtie PhC is located at 1555 nm. It is clear from these results that while the Q of the mixed unit cell PhCs is mildly impacted by the inclusion of the bowtie unit cell, the reduction in mode volume by two orders of magnitude improves the Q/V_m metric dramatically and demonstrates the utility of the mixed unit cell designs, especially with regards to nonlinear optics, advanced sensing, and enhanced quantum emission [46]. While the V_m is similar in all designs with a bowtie at the center of the cavity because the bowtie shape is critical for enabling ultra-low V_m, it is important to note that the Q for all types of PhC nanobeam cavities depends primarily on the number of unit cells and how they are tapered along the nanobeam. Therefore, Q values higher than what we report here are possible by including longer tapers and more maximum mirror strength unit cells.

Table 3.1. Simulated Q and V_m for Mixed Unit Cell PhC Designs

Device	Q	$V_m\ (\lambda/n_{air})^3$
Air Hole-Air Hole	7.9×10^4	1.5×10^{-2}
Air Hole-Bowtie	1.2×10^4	1.6×10^{-4}
Antislot-Antislot	9.4×10^4	2.8×10^{-2}
Antislot-Bowtie	2.7×10^4	2.2×10^{-4}
Bowtie-Bowtie	1.6×10^5	1.9×10^{-4}

The two primary loss mechanisms in a mixed unit cell PhC nanobeam are expected to be air band edge frequency mismatch and mode profile (or impedance) mismatch, the former reducing the effectiveness of the mirrors at the resonant frequency and the latter producing scattering losses at the interfaces between unit cells. Regardless of the optimization method being used, the optimized designs should reflect the intuitive theory of mode coupling between adjacent unit cells. Optimization in Q for both air hole-bowtie and antislot-bowtie designs in Fig. 3.2 and 3.3 show a decrease in the bowtie unit cell width from the period of their respective PhCs. Intuitively, this trend can be understood by considering that the period (a) is related to the vacuum wavelength and effective index (n_{eff}) by $a = \lambda_0/2n_{eff}$, which implies that n_{eff} is larger for the bowtie than the surrounding unit cells. Hence, at a fixed radius, a decrease in the period at the bowtie unit cell (i.e., bowtie unit cell width) is consistent with the principle that the period must be lowered to account for the increased n_{eff} at the same wavelength, λ_0. However, the situation is more complicated when both the radius and width of the bowtie unit cell are varied because the wavelength of the resonance is related to both of these parameters, scaling according to $\lambda \sim a/r$, which can be observed in Fig. 3.2(b, d). The radius of the bowtie unit cell in the mixed unit cell designs must be tuned, as there is a particular radius that produces the best matched air band edge wavelength between the default and functional unit cells. Since the unit cell width and radius cannot truly be tuned independently, it is necessary to find a numerical solution that results in the most efficient coupling of the guided mode between the bowtie cavity and the surrounding mirror segments.

3.4 Experimental results

To experimentally validate the mix-and-match design approach, mixed unit cell PhCs with antislot mirror segments surrounding a bowtie cavity unit cell were fabricated on a silicon-on-

insulator wafer with a 220 nm silicon device layer and 3 μm buried oxide layer using standard electron beam lithography and reactive ion etching protocols, as detailed in Section 2.2.3. In a second lithography step, SU-8 polymer mode couplers were added to improve end-fire coupling efficiency to the PhC nanobeam from the lensed fiber tip used in experimental measurements. Figure 3.4(a) shows a scanning electron microscope (SEM) image of a representative fabricated PhC nanobeam with mixed unit cells. Transmission characterization was carried out on a device with 12 tapering unit cells and 3 end mirror segments using TE-polarized light from a fiber-coupled tunable laser source (Santec TSL-510), tapered fibers (OZ Optics), and a fiber-coupled optical power meter (Newport 2936-C). Figure 3.4(b) shows the measured transmission spectrum with three resonances appearing within the measurement window. The resonance at 1579 nm has a Q of ~4×10^3. The difference in resonance wavelength compared to the simulation is attributed to the dimensions of the fabricated structure differing from those in the simulation and to a different number of tapering unit cells. Fabrication of the bowtie geometry relies on achieving feature sizes as small as 10 – 15 nm at the "knot." We utilized careful multilayer dosing of the bowtie and surrounding features to control the inter-shape proximity effect. While care needs to be taken to fabricate this geometry, the mix-and-match PhC design reduces the number of ultrafine features that get patterned and increases the overall device yield. Moreover, a high-Q resonance can still be achieved even if overexposure of the bowtie knot were to cause an opening in the middle; in fact, an opening at the knot of the bowtie would benefit applications involving, for example, the placement of a quantum dot in the bowtie.

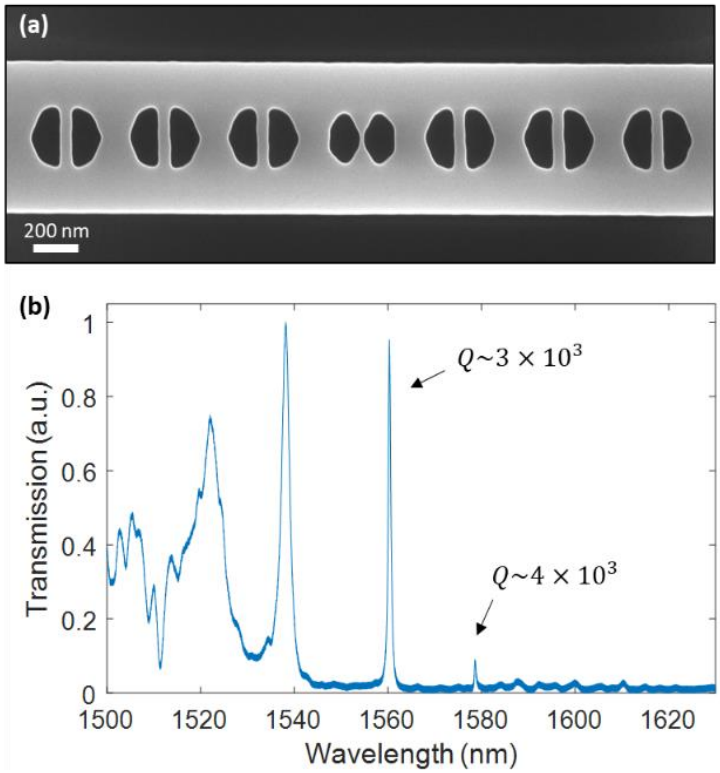

Figure 3.4. (a) SEM image of fabricated mix-and-match PhC with a single bowtie unit cell in the center of a 1D PhC composed of antislot unit cells. (b) Transmission measurement of mix-and-match PhC with a loaded Q ~ 4×10^3.

3.5 Summary

In conclusion, we have shown, through simulation and experiment, a PhC nanobeam cavity that combines the bowtie unit cell geometry with non-bowtie unit cells for low mode volume resonances, demonstrating a method for designing mixed unit cell PhC nanobeams. The achievement of mixed unit cell PhCs is facilitated by the fact that air-mode resonances in PhC nanobeams allow flexibility in adding subwavelength-sized features within the air hole unit cells. Mixing and matching unit cells in a PhC nanobeam provides the PhC designer with enhanced control in crafting the mode distribution across and within individual unit cells to achieve specialized functionality while balancing other competing interests, such as ease of fabrication and

loss-loss operation. Our designed mixed unit cell configuration with antislot unit cells and a bowtie cavity gives high Q/V_m performance ($Q \sim 10^4$, $V_m \sim 10^{-4}\ (\lambda/n_{air})^3$) while reducing fabrication complexity.

CHAPTER 4

Hybrid Si-VO_2 photonic crystal modulator

4.1 Introduction

4.1.1 Background and properties of vanadium dioxide (VO_2)

Fundamentally, an optical modulator functions by dynamically changing the optical properties of a material through which an optical signal is routed. Thus, phase-change materials, which undergo phase transitions and thereby change their optical constants, are highly desirable for use in integrated photonic devices [55], and even more specifically hybrid silicon-photonic modulation platforms [56–58]. One such notable phase-change material is vanadium dioxide, VO_2, which has found great use in optical modulators due to its structural phase transition (SPT) that occurs near room temperature (~68ºC), where the crystal structure changes from monoclinic to rutile. When it undergoes SPT, there is a corresponding insulator-to-metal transition (IMT) of its electronic properties and, with it, a change of the optical constants of VO_2 in the near- to far-infrared [59]. Figure 4.1 displays the rearrangement of the atoms involved in the SPT of VO_2 and how the real and imaginary components of the refractive index change in turn. Compared with similar transition metal oxide phase change materials, it has among the largest changes in optical constants for its relatively convenient transition temperature [60].

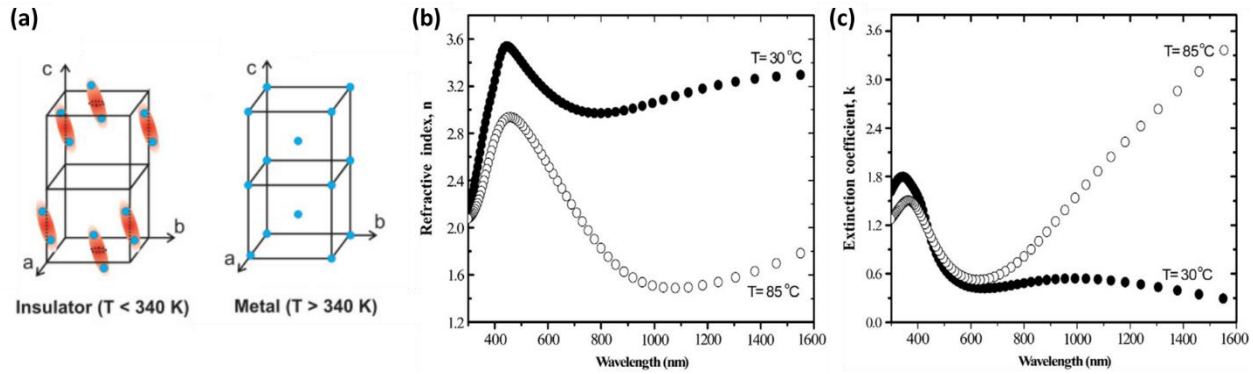

Figure 4.1. Insulator-to-metal transition (IMT) of VO_2 and the corresponding change in its optical properties. (a) Diagram of structural phase transition of VO_2 from a monoclinic to a rutile lattice. Reprinted with permission from [61], © 2012 the American Physical Society. (b-c) Change in the (b) real and (c) imaginary parts of VO_2's refractive index as it undergoes IMT. Reprinted with permission from [62], © 2011 Elsevier.

4.1.2 Hybrid Si-VO_2 optical modulators

The phase transition of VO_2 can be driven thermally, electrically, and optically, so it has found applications in a variety of optical modulator configurations. We have particular interest here in hybrid Si-VO_2 systems that utilize optically-induced IMT for their potential utility in all-optical signal processing and photonic integrated circuits, as well as the picosecond time response that can be achieved (compared to the nanosecond response that can be achieved electrically) [63–65]. Work has been done at Vanderbilt exploring various Si-VO_2 optical modulators, of which two recent platforms [66–69] are shown in Fig. 4.2. In addition, the fabrication of VO_2 structures relies on processing protocols that are consistent with traditional semiconductor fabrication constraints, such as temperature and epitaxy, implying the suitability of VO_2 within the well-established microelectronics and optoelectronics industries [70,71].

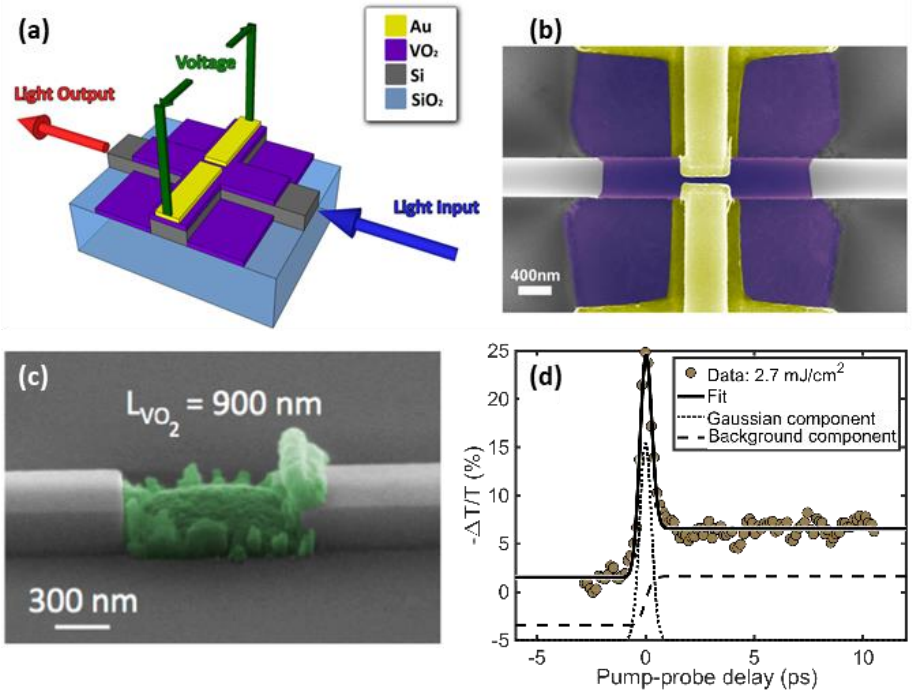

Figure 4.2. Recent past work in Si-VO_2 optical modulators. (a) Schematic and (b) SEM image of the linear absorption electro-optic modulator [66]. (c) Tilted SEM image of a VO_2-embedded Si waveguide optical switch (VO_2 is false-colored green) [67] and (d) sub-picosecond time response of the embedded VO_2-Si optical switch, characterized by pump-probe measurements, the fastest achieved in a silicon platform [69].

4.1.3 Optical modulation with VO_2 integrated on a photonic crystal

The presence of subwavelength features, such as the antislot and bowtie geometries, within the air holes of a PhC nanobeam cavity enables increased light-matter interaction by virtue of the high Q/V_m of the resonant mode that is further confined by interface conditions [13]. Desired here is a higher amount of field interaction with the VO_2 for maximum sensitivity to the IMT. Proposed here is the design and implementation of a hybrid VO_2-Si optical modulator platform built on an antislot PhC nanobeam cavity. The antislot geometry brings some of the same energy redistribution benefits of the bowtie, but with a larger surface area on which to deposit a patch of thin-film VO_2 [13,45,72].

4.2 Design and simulations

4.2.1 Design of antislot PhC cavity

Realizing our optical modulator with a hybrid material system requires considering multiple levels of design factors, including the basic operation of the underlying photonic structure in addition to the careful integration of the phase-change material in a non-destructive, compatible manner. First, a PhC nanobeam cavity with antislot unit cells was designed following the deterministic design procedure [10]. Band edge calculations were performed using MPB, and the PhC nanobeam period was specified at 380 nm, a value chosen to allow for the fundamental resonance to be found near the middle of our desired measurement window of 1500 – 1600 nm while maintaining a high enough n_{eff} to avoid transmission loss into the substrate. It was designed for high-Q resonance, using 15 tapering unit cell pairs and 5 pairs of maximum mirror strength unit cells appended to the ends of the cavity to reduce loss into the 700 nm wide supporting waveguide structure. Each antislot was 50 nm in width, and the fundamental resonance of the cavity was located at 1558 nm with Q = 5.6×10^4. While it is important for the Q to be high enough to enable high switching contrast, there is also a competing risk that the long photon lifetime could negatively impact switching speed if the Q is too high. The PhC was conceived of as operating with a bus waveguide incorporated into the design to allow for side-coupling into the cavity for a high-transmission baseline, so a bus waveguide was included in design simulations for accuracy. A schematic illustration of the device is presented in Fig. 4.3.

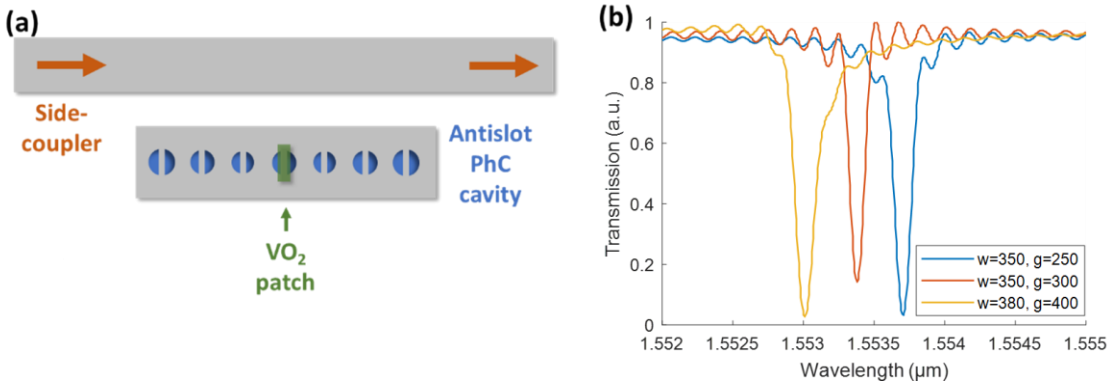

Figure 4.3. Design of VO_2-PhC phase change optical modulator. (a) Schematic of antislot PhC nanobeam cavity designed as a hybrid Si-VO_2 structure. (b) Simulated transmission spectra showing the resonance of the Si-only PhC cavity, side-coupling light into the cavity using several bus waveguide designs. The width of the bus waveguide (*w*) and the coupling gap distance (*g*) are varied in successive simulations.

4.2.2 Side-coupling with a bus waveguide

The previous study done on side-coupling waveguides in Chapter 2 also finds an application in the design of this optical modulator. Because the inclusion of a VO_2 patch lowers the transmission of an otherwise high-Q resonance due to absorption losses that cannot be circumvented, it is prudent to design our device in such a way as to eliminate as much coupling loss as possible, which can be dealt with quite effectively using a side-coupler. By evanescently injecting light into the cavity through an appropriately designed side-coupling waveguide, we establish a high-transmission baseline with resonance depths larger than the resonance peaks of an in-line feeding waveguide [37,49]. The addition of a semiconducting VO_2 patch, then, will decrease the resonance depth (i.e., raise transmission at that wavelength); however, the insertion loss and switching contrast are greatly improved from the in-line case. The PhC cavity now operates similarly to a ring resonator, with switching of the VO_2 causing a sudden increase in transmission at the output.

A simulated sweep of bus waveguide parameters was then performed to determine the waveguide width value and distance from the PhC that provide the best coupling into the cavity, informed by waveguide parameters that were tested previously for another PhC nanobeam cavity in Ref. [37]. The three bus waveguide designs that gave the best performance were a width $w = 350$ nm and gap $g = 250$ nm; $w = 350$ nm, $g = 300$ nm; and $w = 380$ nm, $g = 400$ nm. Figure 4.3(b) shows transmission spectra around the fundamental resonance for all three bus waveguide designs.

4.2.3 VO_2 patch placement

Integrating VO_2 onto a PhC nanobeam cavity with antislot unit cells requires first answering the question of where the VO_2 should be placed for optimal modulation characteristics. Preliminary FDTD simulations were performed with the assistance of undergraduate researcher, Mohammad A. Kabir, to develop intuition about the effect that different VO_2 patch sizes and placements have on the resonant properties of an antislot PhC cavity. We limit our considerations here to VO_2 placed atop the silicon structure due to the fabrication complexities and unwieldy mode interaction caused by VO_2 directly embedded within the waveguide or PhC. Placing VO_2 patches in the dielectric region between the air holes had too weak an effect on the mode to be useful for switching. The antislot PhC nanobeam operates near the air band edge, where the electric field is concentrated inside the air holes, so we position the VO_2 patches atop the antislots directly to ensure an adequate amount of interaction with the field. Upon IMT at 1550 nm, the real part of the refractive index of VO_2 changes from 3.3 to 1.8 with a sizeable increase in absorption, so it might be tempting to introduce patches over many, or all, of the antislots in the PhC to produce maximum field attenuation when the VO_2 transitions to its metallic state. However, the extinction

coefficient of VO_2, even in the semiconducting state, is large enough to produce significant, if not prohibitive, absorption loss with large film areas. This reduces the transmission intensity at the peak of the resonance and, consequently, increases the insertion loss of the optical modulator. An important metric in modulator design that informs us about the switching contrast is the modulation depth, which is defined by the transmission intensity in the semiconducting state (T_s) and the metallic state (T_m), according to:

$$\text{Modulation depth} = 10\log_{10}\left(\frac{T_s}{T_m}\right) \tag{4.1}$$

Simulations of various patch geometries and placements have shown that the most effective design with respect to insertion loss and modulation depth is one in which the VO_2 patches are similar in size to the dielectric bar of the antislot, but also that care must be taken not to extinguish the resonance by the presence of too large a volume of VO_2.

These initial results from tests of different VO_2 patch geometries and placements provide intuition on how the degree of interaction between the VO_2 patch and the resonant mode influences the modulation. FDTD numerical analysis was performed to simulate the transmission spectra through a bus waveguide side-coupled into designed antislot PhC cavity, in order to achieve a practical experimental device. This allowed for the direct quantitative comparison of the figures of merit achieved with different VO_2 patch configurations. The VO_2 patch size was chosen to be 50-nm wide (equal to the antislot width), 250-nm tall, and 70-nm thick. A range of configurations were tested by simulating cases in which patches were located on the dielectric bar of the antislots. When one patch is included at the cavity center in the region of highest electric field concentration, there is a high degree of modal interaction due to the resonant mode's Gaussian attenuation profile across the unit cells. This produces the most dramatic effect when the VO_2 switches to the metallic state, lowering the Q and broadening the resonance because of the increase in its extinction

coefficient and shifting the resonance to a shorter wavelength due to the decrease in its real refractive index. But, conversely, the absorption and modal mismatch due to the inclusion of the VO_2, even in the semiconductor state, lowers the Q of the resonance enough to negatively impact the overall modulation depth during IMT. Thus, greater VO_2 overlap with the electric field reduces Q while increasing the resonance shift. Successive variations where two patches were included, but offset at varying distances from the center of the PhC, were tested in simulation to compare their resonance shift and modulation depth. These results, shown in Fig. 4.4, demonstrate that decreasing the amount of direct modal interaction of the VO_2 can mitigate these losses and increase modulation depth. However, past an offset of 9 unit cells, there are diminishing returns from the Q not growing further while undergoing increasingly smaller resonance shifts, and the modulation depth starts to decrease. A patch offset of 9 unit cells therefore provides the optimal placement of the VO_2, with a loaded $Q = 3.4\times10^4$ in the semiconductor state and $Q = 2.0\times10^4$ in the metallic state. Also tested were asymmetric cases where a single VO_2 patch was simulated at an offset from the center, but these configurations proved to have lower modulation depth than their symmetric counterparts because, while less VO_2 volume might seem to imply less loss, the asymmetry in the mode profile was disruptive for high-Q performance.

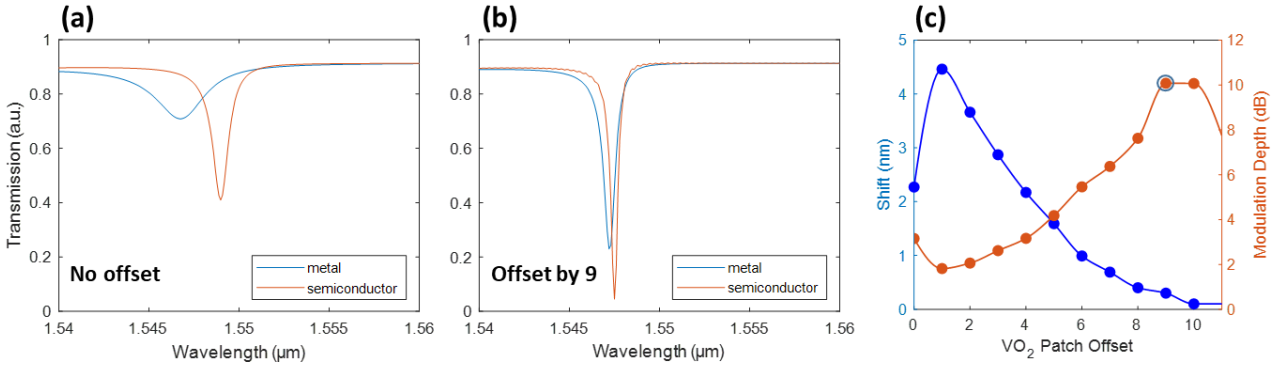

Figure 4.4. Study on the position of VO_2 patch placement and the resulting modulation characteristics. (a) Transmission spectra showing the fundamental resonance of the antislot PhC cavity with a VO_2 patch, in both semiconducting and metallic states, included atop the center of the cavity. (b) Transmission spectra for the antislot PhC with two VO_2 patches at an offset of 9 unit cells. (c) Unit cell offset of VO_2 patches versus the shift in resonant wavelength and the resulting modulation depth.

These metrics are characteristic only of ideal fabrication quality with deposition of the VO_2 directly onto the antislot without any unwanted overhang into the air hole. While this may be possible in simulations, it is not without challenges to realize that level of fidelity to the designed dimensions. Thus, it is beneficial to consider how losses due to fabrication imperfections will affect the modulation performance. This can be clarified by simulating a design case where the VO_2 secondary lithography step results in too large of a VO_2 patch being deposited. In this case, the VO_2 patch that extends beyond the width of the antislot will drape over the dielectric bar of the antislot and into the air hole or lay atop a larger region of the Si waveguide, and the Q of the resonance will consequently be lowered by absorption loss and mode mismatch. Figure 4.5 shows a simulated comparison between the optimized design case discussed above and a modification in which the VO_2 patch was increased from 50 x 250 nm to 150 x 300 nm in size. The part of the VO_2 patch that was larger than the 50-nm wide antislot sat within the air hole atop the SiO_2

substrate. In this design case, the modulation depth decreases to 2.9 dB due to the dramatically lowered Q values of the resonance, both in the semiconductor and metallic states. This highlights the importance of meeting the designed VO_2 patch dimensions as closely as possible in the fabricated structure for high-performance optical modulation. However, the good news is that this simulation may represent a "worst-case scenario" of massive overhang of the VO_2 since a VO_2 patch that is not as oversized, but simply misaligned, may still demonstrate the desired improvement in light-matter interaction due to the antislot geometry while only reducing the modulation performance somewhat from the ideal design.

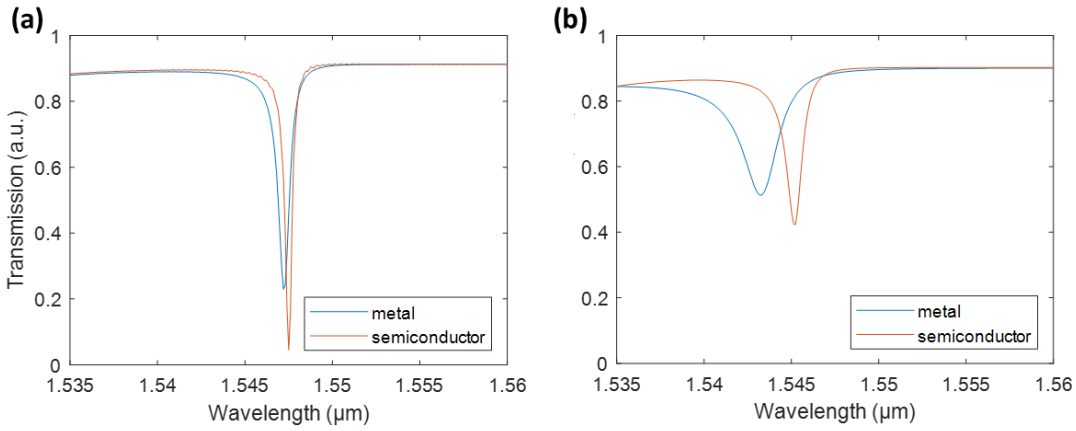

Figure 4.5. The effect of VO_2 patch size and overhang on modulation performance. (a) Simulated transmission spectra for semiconductor and metallic states of VO_2 patches on the antislot PhC cavity, offset by 9 unit cells. (b) Transmission spectra for the same antislot PhC with VO_2 patches at an offset of 9, where the VO_2 patches are increased in size to 150 nm wide and 300 nm tall.

Note that there exists a potential to apply the previous design methodology described in Chapter 3 towards the question of how the VO_2 patches influence the PhC nanobeam resonance. As we saw in Fig. 4.5, the extinction coefficient of the VO_2 will always cause some amount of signal loss, which will be more pronounced as there is more volumetric overlap between the field

and the VO_2. However, insofar as the real part of the refractive index for the VO_2 patches causes a local perturbation of the modal effective index, the dimensions can be modified for the reduction of loss, i.e., higher Q, with the mix-and-match method (cf. Section 3.2). Therefore, if it is found that losses due to certain fabrication imperfections are unavoidable, then this implies that the optimal design and placement of the VO_2 patch unit cells may require modification. While the previously considered design case was to optimize a PhC nanobeam with antislot unit cells modified by a bowtie cavity [72], here we would instead optimize a nanobeam with antislots modified by another antislot with a VO_2 patch on top. It is suspected that the design parameter space for this optimization would be suitable for the use of gradient optimization, which would dramatically reduce the number of simulations required.

4.3 Device fabrication

4.3.1 Fabrication of silicon-on-insulator PhC structures

The PhC nanobeam and feeding waveguides, once designed, were laid out as a device pattern to undergo lithography and verify the design experimentally. Test structures were fabricated on silicon-on-insulator wafers, with the lithography carried out using EBL and RIE steps according to the same procedures used in Chapters 2 and 3. Fabrication was performed at the Center for Nanophase Materials Science at Oak Ridge National Laboratory. Figure 4.6(a) shows an SEM image of a fabricated antislot PhC cavity. Large alignment marks at the corners of the chip and small marks near each PhC cavity were included as part of the device pattern. These alignment marks provide a way to align future lithography steps to the pre-existing silicon structures. However, delays in fabrication due to the evolving COVID-19 pandemic precluded the experimental verification of the simulated design beyond initial fabrication at the time of the

publication of this thesis. Thus, the following fabrication and experimental steps are presented as a roadmap toward this goal.

4.3.2 Deposition of VO_2 films

A secondary lithography step, aligned to the underlying silicon structure, will be completed at VINSE in which EBL will be used to open a window in electron beam resist (950 PMMA A4) with the dimensions of the desired VO_2 patch. Past EBL conditions used for this project were aimed at achieving a low dose of deposited charge of ~350 – 400 μC/cm^2. After exposure and development in an MIBK:IPA solution, a very short O_2 clean of 10 seconds was done to remove residual resist on the silicon surface within the window were VO_2 is to be deposited. RF sputtering at room temperature with a vanadium target and a combination of Ar and O_2 is used to deposit a thin film of vanadium oxide, VO_x. Assuming a proper EBL dose and development time was achieved in the previous steps, a lift-off in acetone should leave remaining a VO_x patch with the designed dimensions sitting atop the surface of the PhC nanobeam. The sample is then annealed in a tube furnace while flowing in oxygen to arrive at stoichiometric VO_2, specifically. Figure 4.6(b) illustrates this fabrication procedure graphically.

Before proceeding to the experiment, the switching characteristics of the VO_2 should be confirmed by using reflectometry on a witness sample to ensure that the film undergoes IMT at the correct temperature. With exceedingly small VO_2 patches, it is likely necessary to deposit an array of appropriately sized patches across the surface of the witness sample so that the switching can be observed in the reflectometry experiment with a reasonable spot size. If the duty cycle of the VO_2 patch array is known, the change in the reflectance upon switching can be calculated to reasonable accuracy.

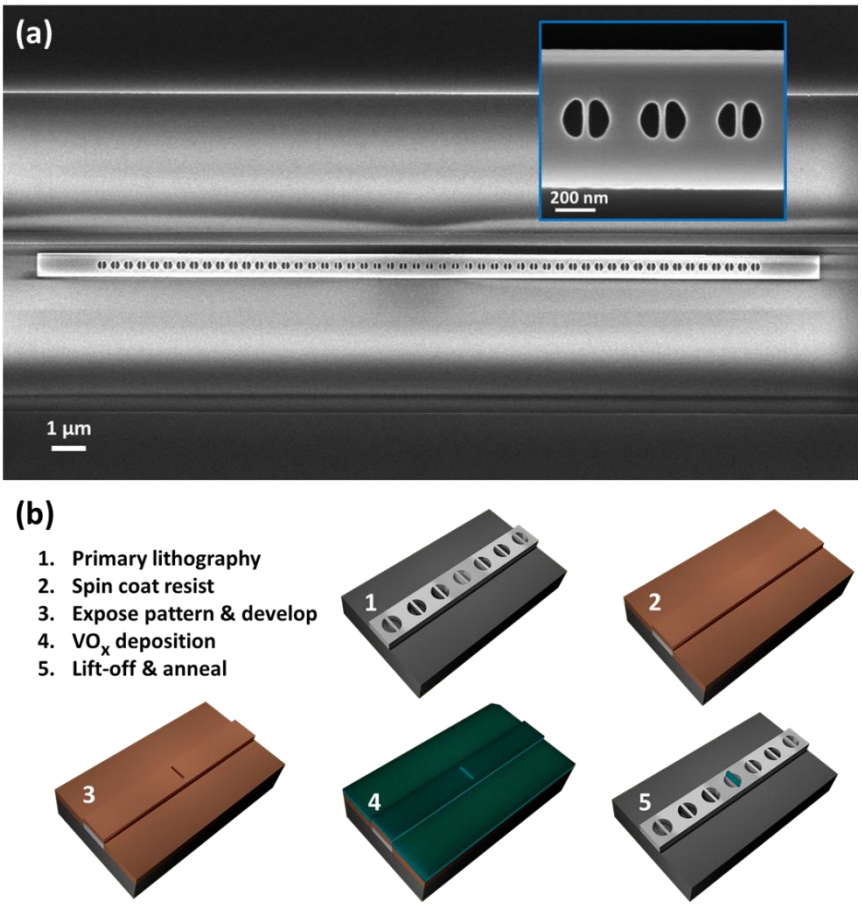

Figure 4.6. Fabrication of VO_2-PhC optical modulator. (a) SEM image of a fabricated antislot PhC cavity with a bus waveguide. All device processing shown was carried out at the Center for Nanophase Materials Science user facility. (b) Illustration of the lithography process for the incorporation of thin-film VO_2 patches on a silicon PhC structure.

4.4 Experimental Procedure

4.4.1 Pump-probe spectroscopy

Due to the speed of the VO_2 structural phase change, measuring the effect of the switching event by simply using a CW probe signal coupled through the feeding waveguide is rendered infeasible by the ultrashort transient time of the signal. It is challenging, or even intractable, to

sample a sub-picosecond switching event by directly transducing the optical signal to an electrical one with a high sample rate, for example with a high-speed oscilloscope.

Thus, pump-probe spectroscopy becomes necessary to probe these physical processes at relevant time scales. Fundamentally, a pump-probe experiment aims to sample a signal in the space domain instead of the time domain. This is done with ultrashort laser pulses by triggering a physical process to occur with a “pump” pulse and measuring some optical property of the process with a separate “probe” pulse. A delay stage is used to control the exact moment at which the pump pulse arrives, and the degree of overlap between the pump and probe pulses allows for the precise sampling of an ultrafast process. The speed of light along the signal path is known, as is the path length, so it is relatively simple to transform between delay state position and pump-probe delay (the operative time unit). A laser pulse traversing 1 millimeter in free space corresponds to around 3.3 picoseconds. Since the delay stage may be controlled very precisely to under a millimeter, this configuration allows for fine temporal resolution in the measurement of the ultrafast dynamics of an optical process.

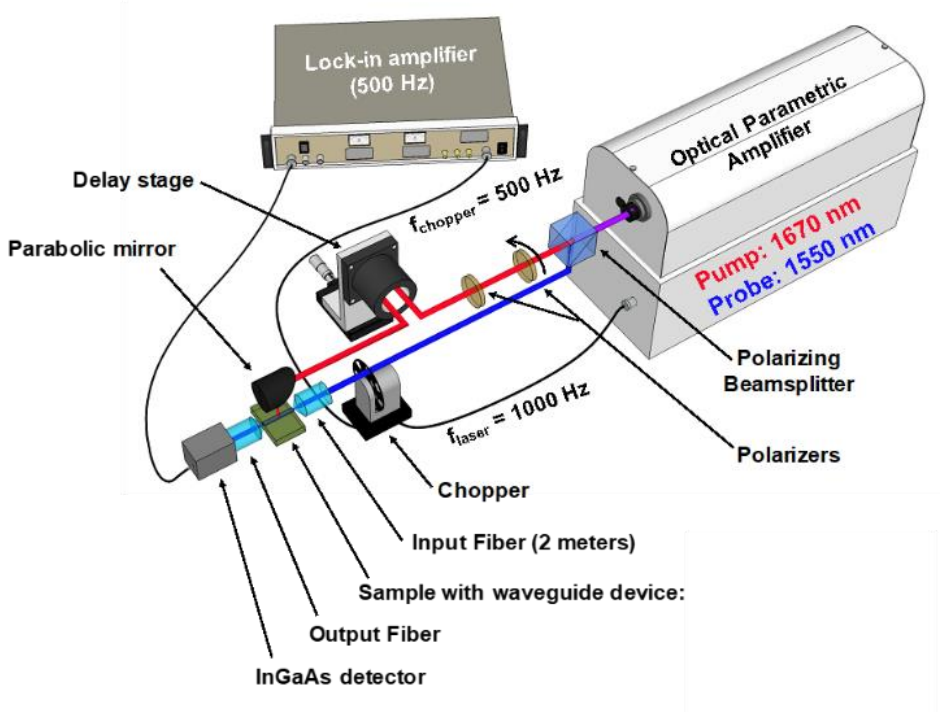

Figure 4.7. Measurement setup for ultrafast pump-probe spectroscopy of VO_2-PhC optical modulator, with out-of-plane pump (OPA idler) and in-plane probe (OPA signal). Image by K. A. Hallman [73].

4.4.2 Experimental setup

Experimentally, optical modulation in this VO_2-PhC platform will be demonstrated and characterized with the ultrafast pump-probe spectroscopy setup shown in Fig. 4.7. This experimental setup is the same as the spectroscopy setup used previously to measure sub-picosecond all-optical switching in a Si-VO_2 waveguide [69,73]. The optical parametric amplifier (OPA) uses a nonlinear process to output two pulses polarized perpendicularly to each other, each of ~100 fs in duration. The repetition rate of these pulses is 1000 Hz. The OPA's signal beam serves as our probe pulse, and the idler beam as our pump pulse. These ultrashort light pulses are separated by a polarizing beam splitter, and they provide the temporal resolution for our measurement. The pump beam moves through two crossed polarizers to control the pump fluence

and a delay stage to control the timing of the pulse with respect to the probe pulse. Finally, a parabolic mirror reflects it onto the sample at normal incidence. With sufficient fluence the pump should induce an IMT of the VO_2, modulating the transmission through the device. To measure the temporal dynamics as the VO_2 patch switches, it is necessary to have the probe pulse travelling in-plane through the waveguide while the process is being pumped. The probe beam is chopped at a lock-in amplifier reference frequency of 500 Hz, half the OPA's repetition rate, and coupled into the waveguide through a tapered optical fiber (via end-fire coupling).

As discussed in the previous section, the temporal resolution of the measurement is a consequence of changing the path length of the pump. The probe pulse, having measured the transient effect of the pump is coupled back into a tapered fiber and ultimately a InGaAs detector whose signal is being amplified by the lock-in amplifier. This signal reveals a transient modulation of the transmission, measured in this experimental setup [69,74] as percentage change from the baseline transmission, i.e., $-\Delta T/T$.

4.5 Conclusions

The optical modulator discussed in this chapter has been designed and simulated, though extenuating circumstances due to the global pandemic have delayed experimentally verifying the design as of yet. The comprehensive simulations done here predict a modulation depth of 10 dB with a hybrid PhC-VO_2 optical modulator. Preliminary results from fabrication agree well with the structural dimension from the simulated design, and further characterization of the transmission spectra will shine light on the utility of this device. Further processing steps of VO_2 will follow, which if successful will be the first incorporation of a phase-change material onto a PhC cavity with subwavelength features (i.e., the antislot). Testing of these structures with the experimental

setup in Fig. 4.7 should ideally demonstrate a sizeable change in the transmission intensity at the output of the waveguide.

Due to the complexity of this modulator platform and its potential for further exploration, this proposed project is conceived of as one phase of a larger series of future study. The most logical next phase would the incorporation of a VO_2 nanoparticle onto a bowtie PhC cavity at the knot of the bowtie. If fabrication challenges with this can be overcome, utilizing an IMT at these ultrasmall feature sizes could even further drive down switching energies and increase switching speed in a modulator. In addition to this consideration of geometry, the VO_2-PhC optical modulator being capable of operating completely in-plane would increase its compatibility with other signal processing components within photonic integrated circuits. To achieve this, it would be necessary to develop robust in-plane pumping.

CHAPTER 5

All-optical switching with a bowtie photonic crystal

5.1 Introduction

We find the basis for the study of nonlinear optical processes by looking at the polarization density, P, of a material and its relationship with an applied electric field [75]. Evaluating this relationship through the power series in the electric field yields:

$$P(t) = \varepsilon_0(\chi^{(1)}E(t) + \chi^{(2)}E^2(t) + \chi^{(3)}E^3(t) + \cdots) \tag{5.1}$$

When the optical field is strong enough, these higher order terms become important and can produce a variety of nonlinear effects that vary with the field. The third-order nonlinear susceptibility term, $\chi^{(3)}$, produces effects in non-centrosymmetric materials that depend on the intensity, I or $|E|^2$, of the electric field.

In the field of photonics, all-optical switching is an appealing goal for signal processing, though one exacerbated by the challenges of weak optical nonlinearity in widely used materials [76]. However, photonic crystals are being utilized as a potential solution, with several attempts at PhC-based all-optical switching being demonstrated in silicon [77–79], GaAs [80], and InGaAsP [40]. Tanabe *et al.* studied one such silicon PhC platform that relied on a simple 2-D PhC nanocavity [78]. Since the field enhancement scales by Q/V_m, a PhC cavity is capable of enhancing the inherently weak nonlinearity of the silicon of which the structure is fabricated. Figure 5.1(a) shows one of their PhC cavity designs, which is coupled to resonant-tunneling PhC waveguides. When a picosecond laser pulse is applied, the resonance shifts to shorter wavelengths, as shown in Fig. 5.1(b).

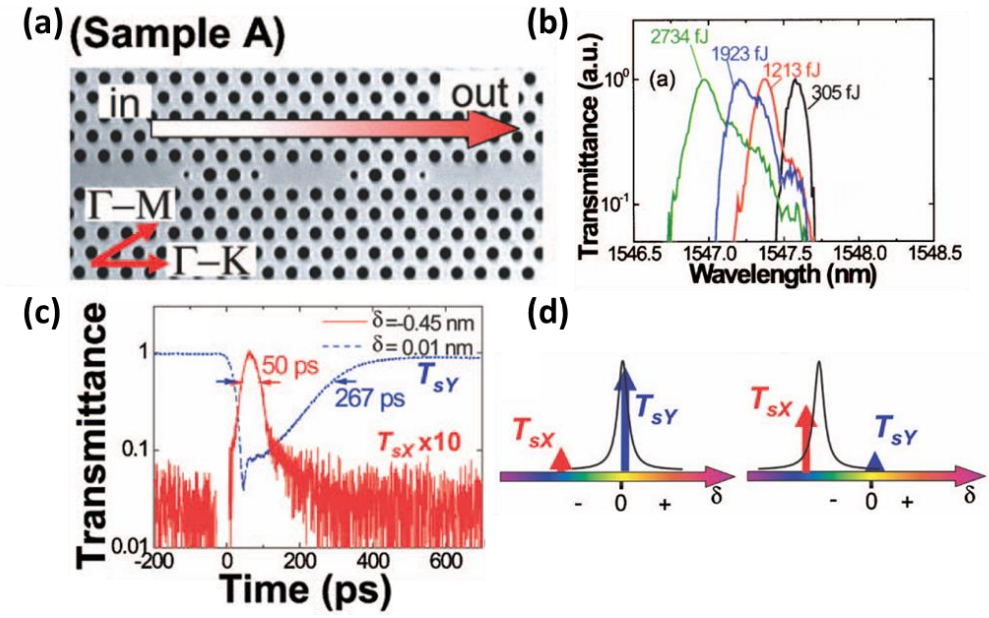

Figure 5.1. All-optical switching implemented in a silicon-based 2-D PhC nanocavity [78]. (a) Fabricated PhC nanocavity. Arrow indicates direction of light propagation. (b) Blue shift of the nanocavity's resonance wavelength as energy of laser pulses (3.7 ps, 10 MHz repetition rate) is increased. (c) Temporal dynamics for all-optical switching of a nanocavity (similar to Sample A) designed with two resonant modes for control/signal isolation. Blue curve indicates on-resonance transmission as the control pulse is applied to generate resonance shift, and red curve indicates off-resonance transmission as the control pulse shifts the signal mode ~0.5 nm away. (d) Schematic of transmission during switching operation at the two measured wavelengths as the signal mode (black curve) is shifted by the application of the control pulse.

The authors attribute this blue shift to a plasma dispersion effect due to two-photon absorption (TPA) generating free carriers. TPA is a third-order nonlinear process that, along with the Kerr effect, can be responsible for an intensity-dependent refractive index change [81]:

$$n = n_0 + n_2 I - i\frac{\lambda}{4\pi}(\alpha_0 + \alpha_2 I) \tag{5.2}$$

In this expression, n_2 is the Kerr coefficient and α_2 is a TPA-induced contribution to the linear absorption coefficient, α_0. It is expected that the contribution due to TPA will be dominant in silicon at 1550 nm telecom wavelengths. Using this effect, a PhC nanocavity similar to the one in Fig. 5.1(a) was tuned to produce all-optical switching at one wavelength by the application of a control pulse at another wavelength. Figure 5.1(c,d) illustrates the switching behavior, where

measuring the transmission at one wavelength allows for a pronounced switching contrast with speeds < 100 ps.

Based on the unique physics at play with the bowtie geometry within a PhC, our goal is to exploit the extreme confinement of light in the bowtie PhC nanobeam to realize all-optical switching based on TPA-induced plasma dispersion, similarly to the work presented above. Since the bowtie PhC has been shown to achieve cavity resonances with $Q \sim 10^6$ and $V_m \sim 10^{-4}\,(\lambda/n)^3$ in simulation (with $Q \sim 10^5$ in experiment), the novel geometry should enable reasonable on-off contrast while reducing the switching energy required. Switching energy is inversely proportional to the Q/V_m field enhancement, and because higher Q results in less of a shift required for switching contrast, the energy reduction scales by V_m/Q^2 [78]. In fact, the previously reported metrics of the bowtie PhC (from simulation) yield $V_m/Q^2 \sim 10^{-16}$, a two order-of-magnitude reduction from the theoretical value calculated by Tanabe *et al.* for a 2-D PhC cavity, which may imply potential sub-femtojoule switching.

The TPA coefficient, β_{TPA}, and the nonlinear refractive index coefficient, n_2, can be normalized for the purpose of comparison of the relative magnitude of the effects. Figure 5.2 shows these trends as a function of the ratio between the light frequency and the band gap. The band gap of silicon is 1.14 eV. Light of 1550 nm corresponds to 0.8 eV (band gap ratio of 0.7), and for 1670 nm light the energy is 0.74 eV (band gap ratio of 0.65). At both of these wavelengths, therefore, the dominant nonlinear process is TPA.

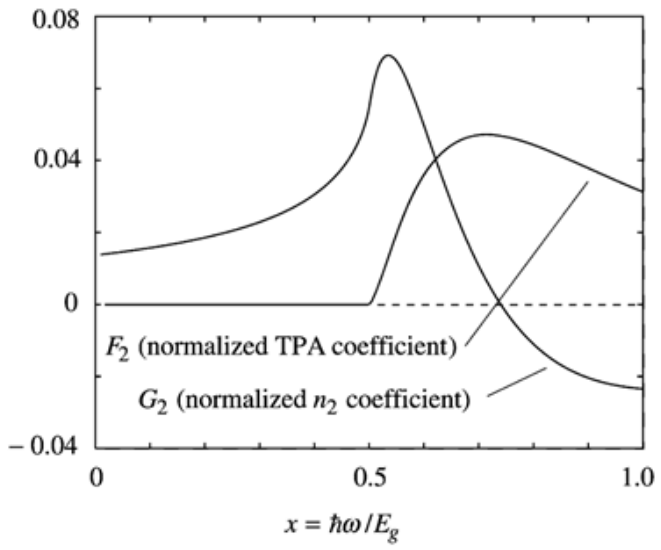

Figure 5.2. Nonlinear coefficients for the nonlinear refraction and two-photon absorption, as a function of the photon energy. Reprinted with permission from [75], © 2008 Elsevier.

5.2 Simulations of nonlinear switching

Linear optical simulations of the bowtie PhC cavity, performed with Lumerical FDTD, reveal key information about the subwavelength mode confinement of the bowtie geometry and its resonance characteristics [13]. This includes the transmission spectrum, Q, mode profile, and mode volume. However, these simulations do not provide information about the third-order nonlinearity of the PhC. Modeling of nonlinear switching due to TPA must be carried out in special FDTD simulations that extend the material modeling functionality that is built into the software package. While the Lumerical software suite does have some basic functionality for modeling nonlinear processes, they are rather limited, and in our case, not extremely useful because it is important to consider exactly how much the resonance wavelength may shift under excitation, which is not well handled by the built-in solutions. Colleague Landen A. Ryder developed an extension to the Lumerical FDTD module to handle nonlinear refractive index due to electrooptic effects, including TPA [82]. With knowledge of the dielectric and the beam profile, it is possible

to calculate the generated carrier density profile. This information can then be imported into the extension to modulate the refractive index accordingly. Such simulations to elucidate the capabilities of all-optical switching using the silicon bowtie PhC are the subject of future work.

5.3 Experimental procedure and ultrafast spectroscopy

5.3.1 Test devices

Already available bowtie PhC nanobeams designed by Dr. Shuren Hu and fabricated by IBM for our previous work [14] make suitable test devices for the observation of this nonlinear refractive index change. Figure 5.3(a-b) shows SEM images and a measured transmission spectrum for one such device. These structures, as is the case with those in previous chapters, were fabricated on silicon-on-insulator wafers with a 220-nm thick silicon device layer. Additional processes steps were performed to deposit SU-8 mode couplers to the ends of the waveguides to enable a 10 dB increase in transmission efficiency during end-fire coupling.

5.3.2 Ultrafast-pump, CW-probe spectroscopy

With adequate simulation and modeling to make reasonable predictions of experiment, an ultrashort pulse laser using light from an optical parametric amplifier (OPA) will be utilized to pump this nonlinear effect out-of-plane, with the desired probe being measured in-plane (i.e., at the end of the output waveguide) by a sufficiently fast photodetector. This is done using a measurement setup similar to that shown in Fig. 4.7, except with a CW tunable semiconductor laser (Santec TSL-510) used to probe the ultrafast optical change instead a femtosecond probe. A fast avalanche photodiode (New Focus 1647) transduces the optical signal, which is then read by a high performance DPO oscilloscope (Tektronix DPO7254C) with high bandwidth and a high

sample rate. This oscilloscope can capture the photodetector waveform as the TPA process is pumped and the transmission is modulated. A specialized LabView program is used to coordinate a sweep of the tunable laser wavelength while recording the oscilloscope waveform at each wavelength. Note, here, that in this version of the ultrafast spectroscopy setup, there is no need for the delay stage since it is not a true pump-probe experiment. Figure 5.3(c) shows a diagram of the ultrafast measurement setup, and detailed instructions for conducting experiment using this setup is included in the Appendix.

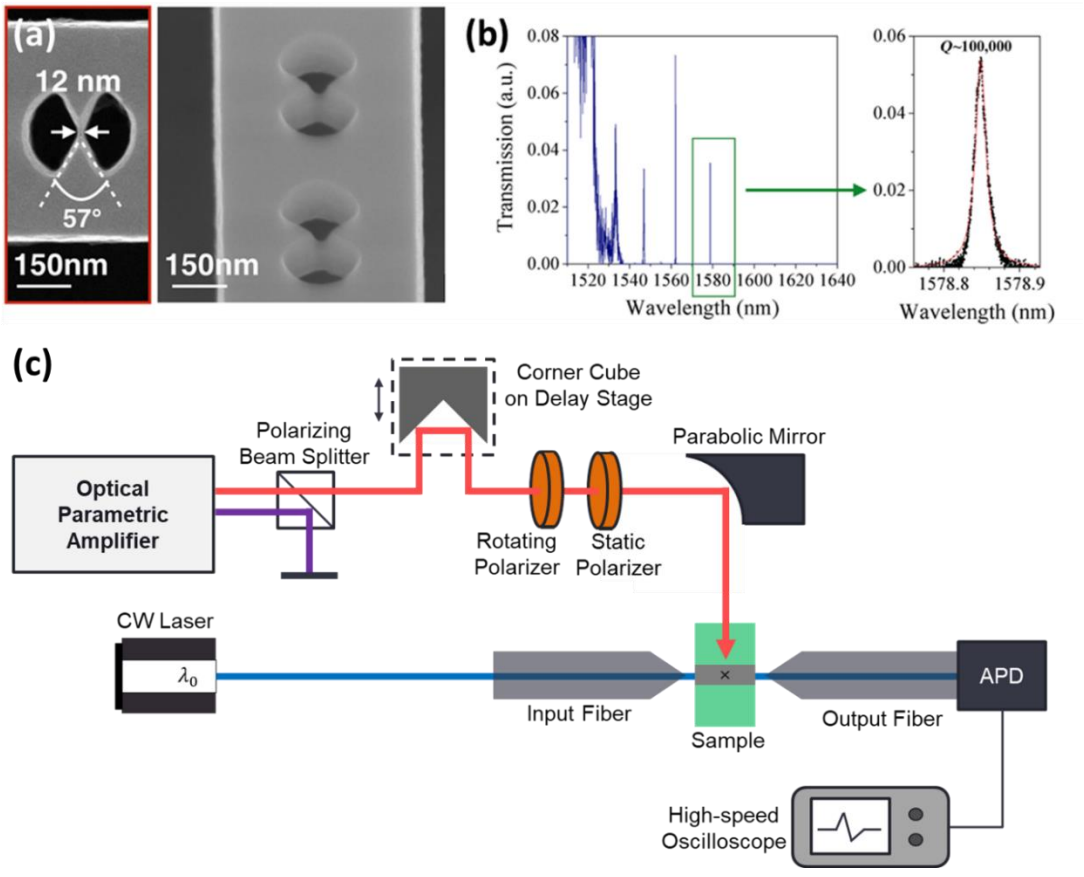

Figure 5.3. All-optical switching experiment performed with a bowtie PhC cavity. (a) SEM image of previously fabricated bowtie PhC nanobeam and (b) representative transmission through one of these nanobeams, showing high-Q resonance (fundamental mode has Q ~ 10^5) [14]. (c) Proposed experimental setup with ultrafast out-of-plane pump (OPA pumped by a Ti:sapphire oscillator & amplifier at 1 kHz repetition rate) and in-plane CW probe.

5.4 Interpretation of results

5.4.1 Data analysis methods

The collection of waveforms we see as the output of this experiment can be very informative about the physical processes that are occurring, but the meaning of the data may not be readily apparent by mere observation. To create a simple example to elucidate the data analysis method, we can create a toy model of a PhC cavity resonance in the transmission spectrum as a Lorentzian peak $T(\lambda) = -\text{Lorentzian}(\lambda; x_0, \gamma)$ where $x_0 = 0$ and $\gamma = 0.5$.

$$T(\lambda) = \frac{1}{\pi\gamma[1 + \left(\frac{x - x_0}{\gamma}\right)^2]} \tag{5.3}$$

When a pump pulse of sufficient intensity is incident on the sample, a change in the refractive index is expected along with a commensurate change in the resonance wavelength (assuming a negligible change in Q). We can model this by considering the wavelength shift as a function of time. The function used will reflect the time response of the nonlinear processes occurring in the dielectric. For a first-order approximation, the wavelength shift in λ can be considered to have a Gaussian shape, $\lambda(t) = \text{Gaussian}(t; \mu, \sigma)$ where $\mu = 1.5$ and $\sigma = 1/\Delta\lambda\sqrt{2\pi}$.

$$\lambda(t) = \frac{1}{\sigma\sqrt{2\pi}} e^{-\frac{1}{2}\left(\frac{t-m}{\sigma}\right)^2} \tag{5.4}$$

This value of σ was chosen to ensure the height of the Gaussian peak is equal to the switching contrast $\Delta\lambda$. Figure 5.4(a,b) display plots of the transmission spectrum, $T(\lambda)$, and the wavelength shift over time, $\lambda(t)$.

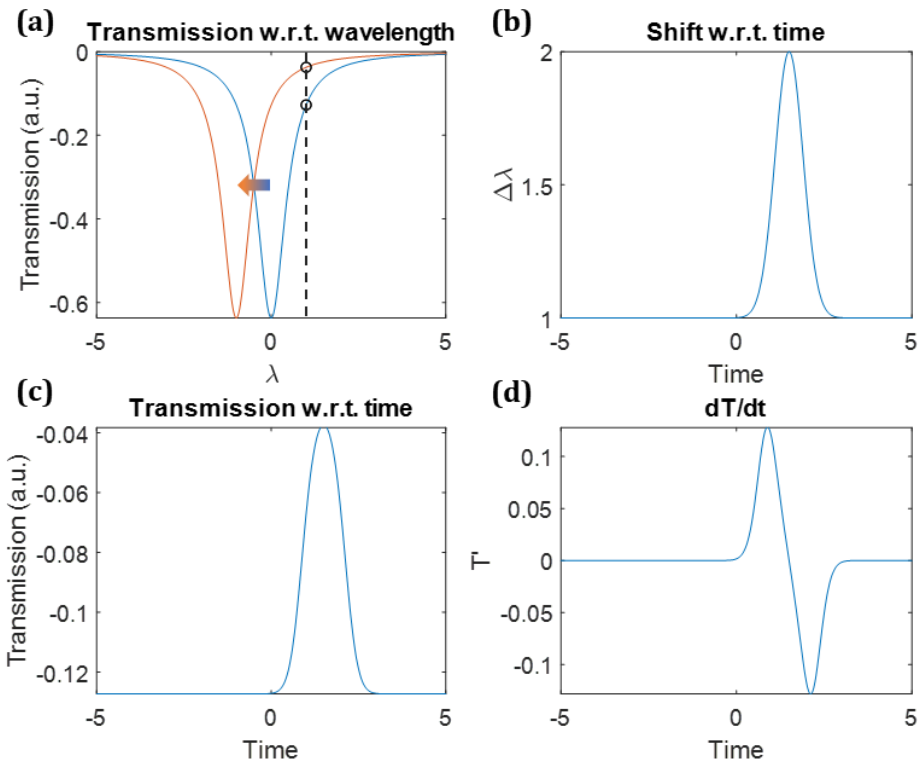

Figure 5.4. Toy model demonstrating the expected photodiode response as the transmission through the bowtie PhC nanobeam cavity is modulated by the femtosecond pump pulse. The initial wavelength here is $\lambda_{init} = 1$. (a) Transmission spectrum as a function of wavelength, $T(\lambda)$. (b) Wavelength as a function of time, $\lambda(t)$. (c) Transmission as a function of time, $T(t)$. (d) Time derivative of the modulated transmisison signal.

As the refractive index of the silicon changes as it undergoes TPA, there is a commensurate change in the wavelength of the resonance. This change in wavelength can be looked at as a shifting of the spectrum to the shorter wavelength side (a blue shift) by $\lambda(t)$. If we measure at a fixed wavelength as this shift occurs, for instance noting the dotted line crossing the transmission spectrum curve in Fig. 5.4(a), when the spectrum blue shifts, the transmission value will increase to that of the orange curve at the same wavelength. This increase in transmission can then be written as $T\big(\lambda(t)\big)$, which is a Lorentzian function acting as the function of a Gaussian.

Figure 5.4(c) plots this modulation of the transmission, which is what we expect to be optically incident on the avalanche photodiode.

However, the photodiode does not purport to directly output a voltage proportional with the incident transmission, but rather the change in the transmission. Thus, we should direct our focus to the derivative of this function $dT(t)/dt$, which is plotted in Fig. 5.4(d). We see here the expected bipolar response of a differentiated Lorentzian or Gaussian function. Note that this response is what we see as the output of the photodiode if the wavelength is first measured at a point on the long wavelength side of the resonance while it undergoes a blueshift. But there are two other import cases to consider. There is also the case where you begin measuring at the short wavelength side, at least one $\Delta\lambda$ shift away from the bottom of the resonance. Now, the positive change in wavelength will cause a decrease in transmission, and the final response will look similar to that of the first case, but inverted.

The final case, shown in Fig. 5.5, is when beginning a measurement at the short wavelength side *less than* one $\Delta\lambda$ shift away, i.e., shifting over the bottom of the resonance dip. This has the interesting consequence that the photodiode output will now have two peaks (and two dips) since the transmission will initially decrease, then increase, then decrease, before finally increasing again. The surprising consequence of this is that, if the photodiode is truly providing a view of the time rate of change of the switching, it might be possible to directly read off the magnitude of the wavelength shift by observing this multipolar curve in its output.

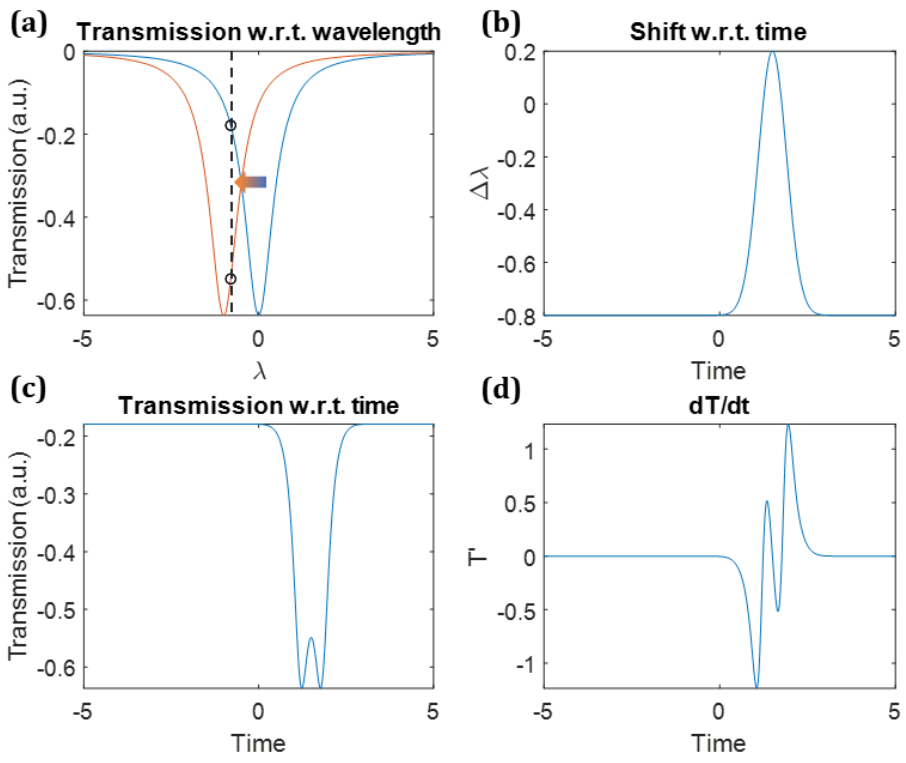

Figure 5.5. Toy model of the photodiode response for the nonlinear bowtie PhC experiment, showing a wavelength shift over the PhC resonance, i.e., initial wavelength $\lambda_{init} = -0.8$. (a) $T(\lambda)$. (b) $\lambda(t)$. (c) $T(t)$. (d) $dT(t)/dt$.

5.4.2 Results

First, in order to establish a baseline of performance, experiments were initially conducted with a silicon ring resonator, whose switching behavior in a similar ultrafast optical setup was studied previously by Dr. Kent Hallman and Dr. Judson Ryckman [73]. The pump pulse is a Gaussian spot on the surface of the device (at normal incidence) with a wavelength of 1670 nm, pulse duration of 130 fs, and beam diameter of 70 μm (e^{-2}). FDTD simulations designed to account for the nonlinear effect of TPA suggested switching would occur with an index change of 3×10^{-3} upon the application of the pump pulse producing a carrier density of 1×10^{18}.

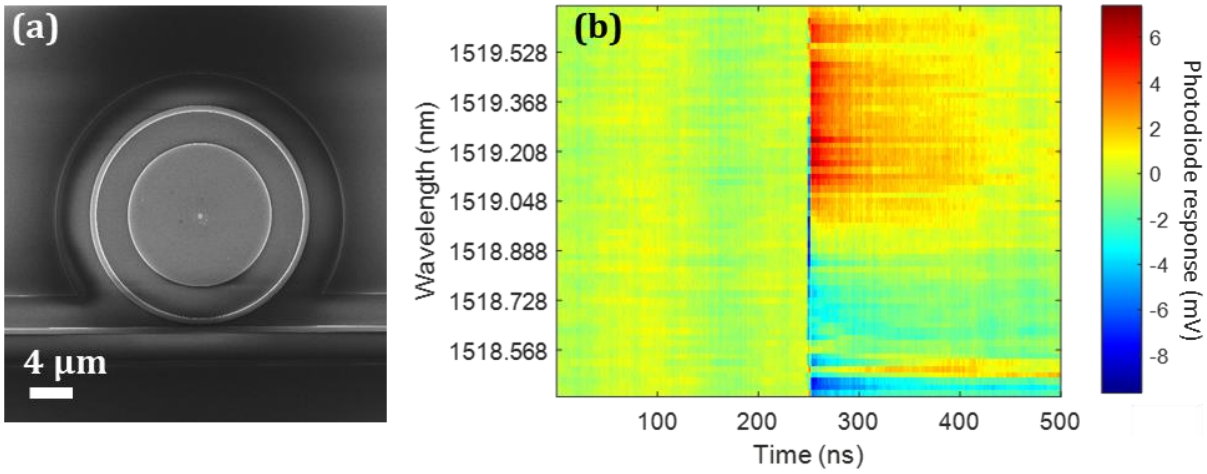

Figure 5.6. All-optical ultrafast switching experiment with a silicon ring resonator. (a) SEM image of ring resonator. (b) Sweep of the CW probe wavelength, capturing the oscilloscope waveform of the photodiode response at each wavelength and an apparent switching event past $t = 250$ ns. Photodiode response data is adjusted by subtracting a pump-only waveform from the measured pump-probe waveforms.

A previously fabricated ring resonator sample (representative image shown in Fig. 5.6(a)) was utilized in an ultrafast switching experiment as described above. The fluence of the pump was changed from 10.3 to 54.0 mJ/cm^2 to determine if a threshold for switching behavior could be identified, alongside any other important physical processes. At each fluence value, the tunable laser was swept across a range of wavelengths around the resonance minimum (keeping in mind this is a side coupled device) while the oscilloscope waveforms were being automatically recorded. Afterward, these collections of waveforms are then laid out across the spectrum to visualize the photodiode voltage as function of time and wavelength in a two-dimensional plot. It is also possible to use these photodiode response data to modulate previously captured (by straightforward, low-power CW measurements) transmission spectra in order to directly show how the spectrum must apparently be changing on the time scale of the ultrafast spectroscopy. Experiments with the ring resonator seemed to show a switching event occurring beyond a fluence of 35.0 mJ/cm^2. Figure 5.6(b) shows the change in time of the photodiode response, with the residual signal of the

pump coupling into the waveguide and influencing the transmission having been subtracted out. Observing the color of the regions around the resonance wavelength $\lambda = 1519.048$, it appears to show the expected signature of TPA-mediated switching for this device, which is an increase in transmission at wavelengths longer than the resonance minimum and a decrease at shorter wavelengths as a blue shift occurs (cf. Fig. 5.4 and Fig. 5.5).

With this positive result of switching with the ring resonator, a similar experiment was attempted with a bowtie PhC cavity. The CW transmission spectrum was measured to acquire the location of the fundamental resonance, and the same procedure was followed as before, but unfortunately sweeping the fluence of the pump across a wide range, even to extreme values, did not seem to trigger the switching response that was expected. That is to say, there was no signature of switching in the photodiode waveforms, just a consistent baseline of zero (change) across the spectrum before and after the incidence of the pump.

5.5 Outlook and future experiments

These results highlight the fact that, while the bowtie PhC exhibits exceptional energy enhancement, it is still quite challenging to access the energy density at the knot of the bowtie [83]. Due to the out-of-plane pumping of the cavity, there is a fundamental limit on how much optical energy can be absorbed via TPA into the silicon of the bowtie PhC cavity. While the work shown here involves out-of-plane pumping of the nonlinear process, comparable attempts at nonlinear switching of PhC devices utilized in-plane pumping, injecting light through the same feeding waveguide through which the probe is operating [78,84]. Thus, the next logical step in investigating nonlinear switching of the bowtie is to likewise adapt the experiment towards in-plane coupling. In addition, there could be value in working at different pump wavelengths, for

example wavelengths within the band gap of silicon. This potential move to the linear regime demonstrates different physics but could still allow all-optical switching of the bowtie PhC to be demonstrated.

CHAPTER 6

Conclusions

6.1 Summary

Optical signal processing is a crucial field for meeting our growing information needs, and the work done in this dissertation aims to develop the fundamental science and engineering necessary for creating practical photonic solutions. Photonic crystals are envisioned here as a building block for components of photonic integrated circuits, and their use in resonant optical cavities can provide a versatile platform for the creation of nanoscale optical modulators to encode and decode signals with light. We approach this by tailoring the PhC properties for enhanced manipulation of the propagation of light. In this dissertation, focus was given to developing PhC design strategies in order to enable functional optical modulators to be realized with competitive performance metrics. First, design techniques for engineering integrated PhC nanobeams were presented that provide a basis to achieve high-transmission, high-Q resonance using side-coupling and that demonstrate a new method for creating mix-and-match PhC cavities, which incorporate multiple unit cell geometries within a single device. Furthermore, novel optical modulator platforms were proposed and explored by combining the unique resonant properties of designer PhC cavities with techniques for switching the optical properties of the modulator. This was done using VO_2 and the inherent nonlinear optical phenomena of the dielectric from which the PhC is made. A hybrid Si-VO_2 PhC cavity platform for optical modulation was designed and simulated by carefully incorporating small patches of VO_2 onto a PhC nanobeam to control the wavelength and quality factor of its resonance, and thereby achieve a simulated modulation depth of 10 dB. Finally, a bowtie PhC cavity geometry for possible all-optical switching was explored in theory

and experiment, motivated by the potential of the exceptional Q/V_m ratio in the bowtie to reduce the energy required for switching.

6.2 Outlook and future avenues

There are many directions in research and application that the work presented here could lead to in the future, and it is my hope that the progress made in these projects can serve as a foundation for the development of useful technologies in the fields of optical communication and information processing. Silicon photonics looks very promising in its ability to provide practical, scalable solutions in these areas, relying upon well-established fabrication capabilities to move analogous devices into the optical domain or to expand already existing optical engineering (e.g., fiber optics and optical interconnects). Optical modulation strategies, such as the approaches studied in this dissertation, are being employed in high-performance computing and to combat a bottleneck in the performance of interconnects between separated integrated circuits. As the natural extension of optical switching using integrated photonics, photonic computing is likewise being broadly investigated since less energy would be required to achieve high-bandwidth processing compared to traditional computing.

In quantum computing and quantum information processing, there is also a push towards photonic approaches being investigated by several startup companies and established names, such as IBM. Some of this work is in applying photonics towards the long-distance transmission of quantum information, motivated by the robustness of optical information against loss, while other work seeks to directly apply optics for quantum computing using a "photonic cubit." There are also other avenues of research, such as LIDAR, information storage, and optical display technologies. In all these areas, integrated photonics is immediately applicable to control and

manipulate the state of light, and photonic crystals – I would argue – are an important part of a photonic designer's toolbox to create useful optical solutions to real-world problems.

Appendix

A. Spectrum-resolved measurement with the ultrafast setup

A.1 Introduction

The experiments discussed in Chapter 5 for probing all-optical nonlinear switching of a bowtie PhC involve performing spectrum-resolved measurements with a femtosecond pump and a CW probe. When an ultrashort pump pulse is applied to the sample out-of-plane, this setup is designed to capture changes in the transmission intensity through the device waveguide at finely resolved wavelength steps within the transmission spectrum. The data captured by this experiment are an ensemble of time-domain oscilloscope waveforms at the moment the pulse arrives, recorded at each wavelength in a user-defined sweep across the spectrum. Thus, in a way, this experimental technique provides both time- and wavelength-domain information about a potential switching event, though it should be noted that the time-domain information is deprioritized by this method because of the inherent bottlenecks in response speed due to the equipment being used, in addition to the fact that this is not a true pump-probe technique. For a more accurate picture of the timescales within which VO_2 phase transitions may occur and modulate a photonic structure, refer to the pump-probe technique intended for the project discussed in Chapter 4 and used previously for measuring optical modulation of Si waveguides with embedded VO_2 in prior work [69]. The experimental technique used to accomplish the studies conducted so far was adapted from the experimental procedure used by Dr. Kent Hallman in these works [58,69,73].

This appendix will highlight in detail the steps required to conduct these wavelength-resolved ultrafast measurements, and hopefully establish a baseline in experimental technique

upon which future modifications can be made in order to increase the amount of energy absorbed by the Si structure or to resolve smaller switching signatures in the signal.

The steps in the experimental procedure highlighted below are to first start up the ultrafast laser amplifier which feeds the optical parametric amplifier (OPA) [Section A.2], then perform the alignment of optical fiber tips to the device waveguide to feed in CW light [Section A.3], align the optics in the femtosecond pump beam path [Section A.4], and align the pump beam spot onto the device [Section A.5]. Then, an explanation is provided for the practical considerations of pump fluence and polarization, and the steps for running a sweep and capturing experimental data are detailed [Section A.6]. Finally, a shutdown procedure is provided to safely turn off each piece of equipment when experiments are completed [Section A.7].

A.2 Start up the Ace system

Before conducting experiments, the first step is to start up the Spectra-Physics ultrafast amplifier-OPA setup. A block diagram of the entire setup is presented in Fig. A.1 to illustrate the basic arrangement of the constituent optical equipment. This consists primarily of the Spitfire Ace system and the auxiliary equipment required for its operation. The TOPAS OPA, which provides the signal and idler pulses for an experiment, is a primarily passive component that should need no major adjustments. If it is found after proceeding with all of the process steps outlined in the following text that the OPA does require adjustments (e.g., due to a mismatch between measured wavelength and set wavelength, or anomalously low power), ensure that all necessary laser safety protocols are followed and, preferably, consult with the expertise of someone more familiar with the intricacies of the Ace system or OPA's operation. Prof. John Kozub is a valuable resource with much experience who may be consulted if specific concerns arise.

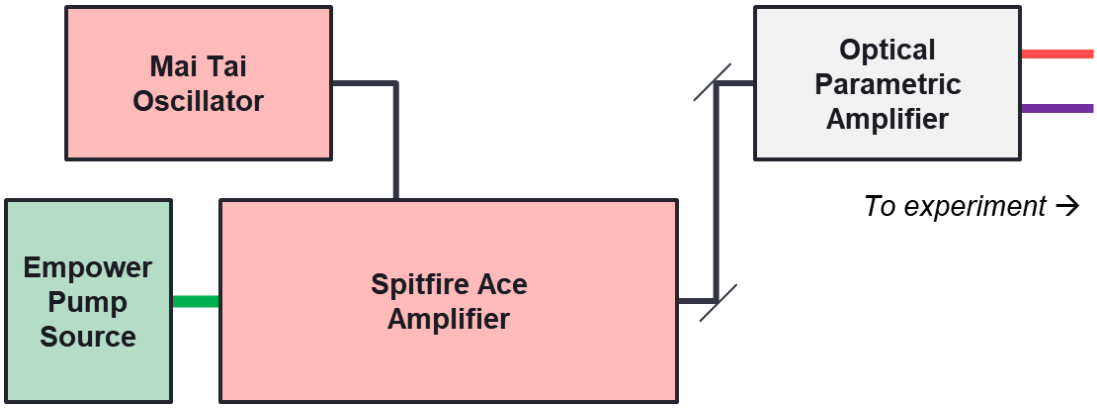

Figure A.1. Block diagram of the Spectra-Physics ultrafast amplifier-OPA setup. The Empower Q-switched green laser, serving as a pump source, and the Mai Tail short-pulse oscillator feed the Spitfire Ace Ti:sapphire regenerative amplifier to produce ultrashort pulses at 800 nm. The TOPAS optical parametric amplifier (OPA) generates signal and idler pulses at near-infrared wavelengths, which can then be used for ultrafast spectroscopy experiments.

Follow the below steps to start up the Spitfire Ace system:

1. Turn on the oscilloscope next to the Spitfire Ace system.
2. Power on the TCU, Empower, and TDG controllers using the power switches on the front panel of their respective rack-mounted units.
3. Let the Empower warm up for 10 minutes before proceeding.
4. Start the Spitfire Ace software using the icon on the desktop and click on “Connect to System.”
5. Turn the interlock keys for the Empower and TDG to the “ON” position.
6. After the Ace software has finished loading, clear any active errors in the “Active Faults” tab of the program.
7. In the software, hold the Mai-Tai “ON/OFF” button and wait for full power indication.
8. Open the Mai-Tai shutter and click on “Reset PD.”

9. Hold the Empower “ON/OFF” button and wait for full power indication.
10. Verify correct delay settings for CH1, CH2, and CH3. Shorter times can be used for CH3 to reduce the power output, but avoid modifying this if you do not know what you are doing.

Table A.1. Regenerator delay settings

Channel	Delay
CH1	80.5 ns
CH2	102.0 ns
CH3*	212.25 ns

11. Click on the switch to turn the Regen on.
12. Wait at least 15 minutes for the system to warm up, then optimize the compressor length. If necessary, set the motor for “Manual Control” and adjust the motor position while watching the power as measured at the output of the OPA. Choose the motor position that will maximize the power for the experiment.
13. The OPA power should be above 200 mW ideally. If the motor position is at its optimal value and the OPA power is still low, try adjusting the mirror mount at the input of the OPA to ensure the beam is properly aligned into the unit.
14. While not a part of the Spitfire Ace system, it is important to take an opportunity early in the course of the experiment to turn on the DC power supply which powers the New Focus 1647 avalanche photodiode (APD). Ensure that it is set for ±15 V as specified in the equipment manual for the APD. This is done to allow the unit to warm up for an hour to thermally stabilize before performing measurements and does not necessarily need to occur in the order written.

A.3 Align fiber tips

The Poynting vectors of the signal and idler beams from the OPA will tend to drift as the setup warms up, so it is expedient to perform alignment of the fiber tips to the waveguide facets with the CW laser in the meantime before aligning the pump pulse beam path. This alignment procedure follows the standard protocol used for performing end-fire, fiber-coupled transmission characterization, as was done in the experiments described in Chapters 2 and 3. Note that the infrared camera in this setup is positioned at a 45º angle to the surface of the sample to allow for normal incidence of the pump beam. Alignment of the fiber tips thus requires working with an oblique plane of focus in the camera view, which results in only one or two waveguides being in focus for a given sample position.

1. Mount the sample on the brass sample holder using carbon tape, and carefully slide the sample holder to position the sample between the fiber tips without making contact between the sample and the fibers. Try to position the sample so the waveguide of interest is aligned to the fiber tips.
2. Turn on the 3-axis piezo controller, which drives the piezoelectric actuators that are used for fine-precision movements of the fibers. Wait a moment for the unit to adjust the actuators to their previous position, then change the position of each axis to 50 at the center of the range.
3. Turn on the fiber illuminator, the camera, and the monitor. While watching the camera image in the monitor, adjust the camera micrometers to move the image over the waveguide of interest and to adjust the focal plane so the waveguide is in focus.
4. Once the surface of the sample and the waveguide of interest are in focus, adjust the left (input) fiber in and out of the plane of focus (the z-direction as marked on the input side of

the measurement stage) until the fiber tip is resolved with the same focus as the waveguide. This indicates that the fiber tip is roughly aligned to the silicon device layer of the chip.

5. Ensure the input fiber is connected to the tunable CW laser via a fiber patch cable, then turn on the laser. Once the laser has warmed up and the laser diode is active, start with the lowest power setting necessary to enable alignment so that there is no risk of damage to the device (specifically in the case of thermally sensitive PhC cavities).
6. Move the input fiber laterally along the edge of the chip while maintaining a safe distance so the fiber tip does not touch the chip and align the fiber tip to the facet in this axis (the x-direction as marked on the stage).
7. Adjust the input fiber in and out of the plane of focus in the z-direction, as before, until the desired waveguide illuminates with scattering down the waveguide, indicating that the fiber tip is roughly aligned to the facet and injecting light into the waveguide.
8. If the input fiber tip is roughly aligned in the x- and z-axes and there is sufficient light reaching the end of the output-side waveguide, proceed to attain rough alignment of the right (output) fiber tip. If there is still not enough light to align the output fiber, very carefully move the input fiber in towards the sample with its y-axis micrometer, being abundantly cautious not to move it too close or crash it into the edge of the chip.
9. As done in Step 4, in adjust the output fiber in and out of the plane of focus (the z-direction as marked on the output side of the measurement stage) until the fiber tip is resolved with the same focus as the waveguide.
10. Connect the output fiber to the probe power meter, a red handheld Thorlabs unit with an attached InGaAs detector. When not in use, ensure this power meter is turned off to conserve battery power and is reconnected to its charger. Be extremely careful in handling

the output fiber, as overbending could result in the fiber snapping and pulling it could yank it out of the fiber mount.

11. Move the output fiber laterally along the edge of the chip while maintaining a safe distance and align the fiber tip to the output waveguide facet in this axis (the y-direction as marked on the measurement stage). Note the change in the axis designation on the output side, as compared to the input side.
12. With the probe power meter turned on, adjust the input fiber in and out of the plane of focus in the z-direction, as before, until a measurement signal can be read out on the power meter display. Slow movements might be necessary to align adequately to the very thin silicon device layer.
13. Once a rough alignment attains measurable transmission at the output waveguide, it is time to proceed to fine alignment of the fiber tips. Without moving the fibers closer, optimize the power reading by using the knobs on the piezo controller to move the input and output fiber tips into more optimal alignment. This requires the x- and z-axes for the input side and the y- and z-axes for the output side. Do not adjust the input side y-axis or output side x-axis yet, both of which are covered by sticky notes.
14. Once the lateral alignment is optimized for both fiber tips, you may proceed to adjusting the distance of each fiber from the waveguide facets. Because the camera is only viewing the stage with a 5x objective, there is a fundamental limit to how well the distance can be resolved by eye, so it is important to be gentle and methodical here to prevent from crashing the fiber tips into the sample or otherwise damaging them and the waveguide facet.
15. Adjust the input side distance with its y-axis knob on the piezo controller to maximize the power reading. If the power starts to decrease as you move it closer, do not bring in the

fiber tip any further. If you reach the maximum position of the piezo controller knob and the power is still increasing, then note that power reading as a likely safe position, reduce the piezo controller position to a lower number, and manually adjust the coarse micrometer until you achieve that power reading again. Then proceed to adjust the piezo controller and repeat this step until the power no longer increases when bringing the fiber tip closer.

16. Follow the same procedure as Step 15 for the output fiber. Adjust the output side distance with its x-axis knob on the piezo controller and readjust with the micrometer if necessary, as before, until you reach the peak power reading possible.
17. It may be necessary to touch up the input and output side lateral alignments if they have drifted. Once you are confident in having achieved the optimal alignment, record the power reading at the wavelength of interest in your lab notes.
18. Use a marker to mark the location of the device (as discerned by a bright spot in the image due to scattering) so that the pump spot can be aligned to that feature in the next stage of the experiment.
19. Disconnect the probe power meter and connect the output fiber to the APD that is interfaced with the high-speed oscilloscope.

A.4 Align pump beam path

To properly align the pump beam path, it is important to carefully ensure the entirety of the OPA idler is reaching the parabolic mirror with as little unwanted attenuation as possible from misalignment. Accomplishing this requires following the two-mirrors, two-irises technique. This involves setting up irises downstream of two mirrors that one would like to align. The first mirror is adjusted to align with the first iris, and the second mirror is adjusted to align with the second

iris. Iterating through every mirror in the beam path in this way should result in properly aligned optical system.

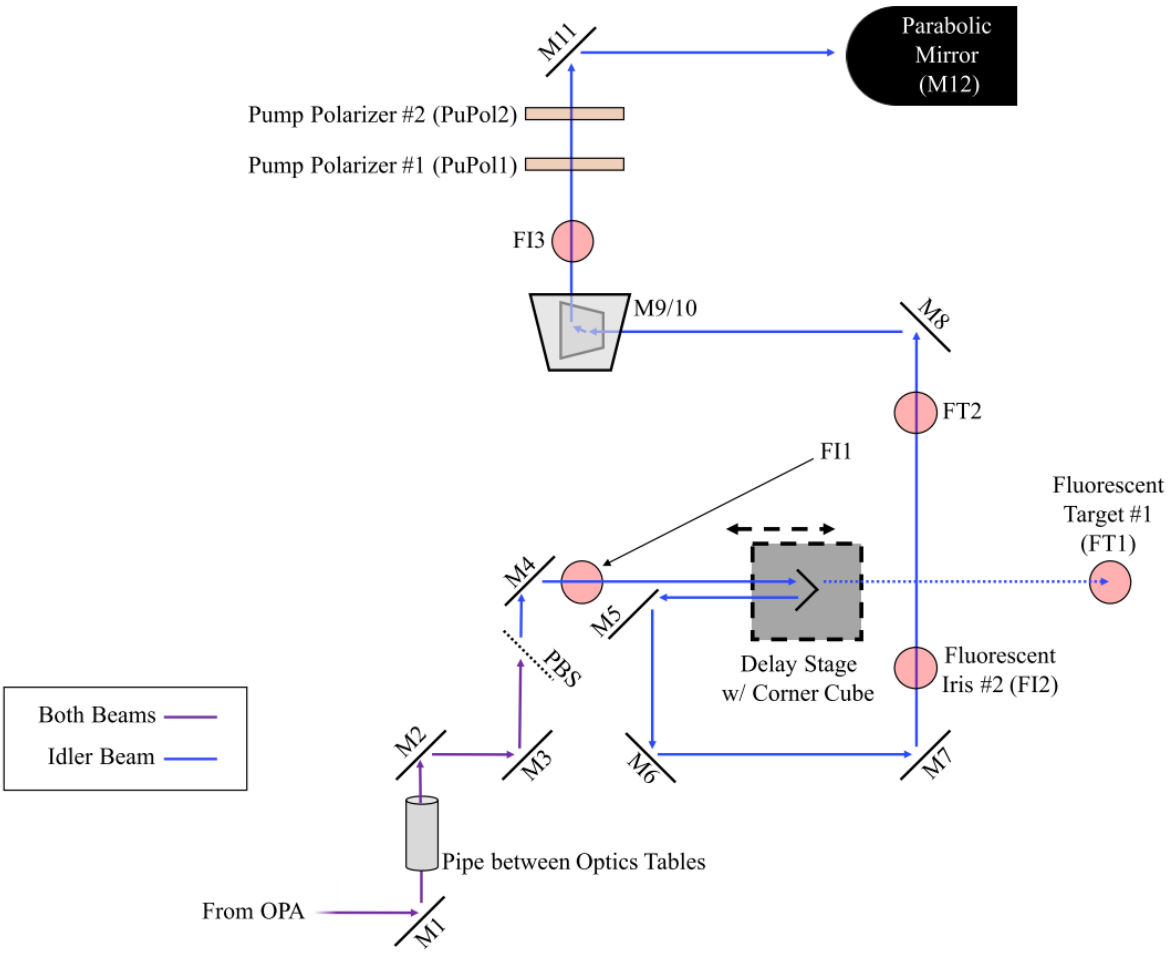

Figure A.2. Plan view schematic of out-of-plane pump signal path, using the idler beam of the OPA. Dotted blue line represents idler beam in alignment steps. Fluorescent iris and target indicators represent the mounts where the fluorescent alignment disks should be placed during the appropriate alignment step. Abbreviations are defined in the text. Not drawn to scale. Adapted from [73].

1. Ensure that the sample is blocked from an incoming pump beam by flipping up the pyroelectric power meter that is on a flip mount ahead of the parabolic mirror.

2. Procure a flashlight and turn off the room lights.
3. Use a fluorescent detector card (Thorlabs VRC2) to check that the OPA beam is incident on the center of mirror #1 (M1). Unless a long time has passed since previous experiments or there has been significant vibration on the optics table, this should not need adjustment. However, if the beam is not center on the mirror, block the OPA and adjust the mirror mount while maintaining a 45^{o} angle on the optics table for M1.
4. Check that the beam is hitting the center of mirror #2 (M2) and mirror #3 (M3). If the beam is off-center for one, adjust the knobs of the previous mirror in the beam path.
5. Check that both the signal and idler beams are passing through the opening of the polarized beam splitter (PBS). If the 1670-nm idler, which is our pump beam, is indeed passing through the PBS, it should not be visible when using a VRC4 detector card, which has a cutoff wavelength of 1590 nm. The OPA signal beam should be reflected by the PBS.
6. Check that the beam is hitting the center of mirror #4 (M4) and, if not, adjust the knobs of the M3 mirror mount. Note that it is unlikely that adjustments will be needed for steps 3 – 5 if the experimental setup has been used recently and the optics aligned.

Note that we will now proceed with using the two-mirrors, two-irises technique.

7. Without unscrewing, moving, or adjusting the mount, put fluorescent iris #1 (FI1) into the mount and screw it into place. Mount fluorescent target #1 (FT1) at the other end of the optics table segment in the same way as FI1.
8. Remove the corner cube from the delay stage by gently rocking it toward you so that it is not pulled strongly toward the table by its magnetic mount and knocked out of alignment.

9. Align the mirrors M3 and M4 to FI1 and FT, respectively. Adjust the M3 knobs to center the beam within FI1, and the M4 knobs to center the beam onto FT1. Then iterate back and forth between M3 and M4 until the beam is simultaneously aligned to both FI1 and FT1.
10. Replace the corner cube in into its position by gently tilting it back onto the table without letting the magnet mount pull it violently to the table.
11. Check that the beam is properly reflected from M4 to the corner cube to the pickoff mirror, mirror #5 (M5). Readjust the previous mirrors if this is not the case; however, do not modify the corner cube or the pickoff mirror M5.
12. Install fluorescent iris FI2 and move fluorescent target from FT1 to FT2.
13. Align the mirrors M6 and M7 to FI2 and FT2, respectively, in the same manner as Step 9.
14. Remove all the irises and targets.
15. Check that the beam is centered on mirrors M8, M9, and M10, and within the measurement box check that it is centered on pump polarizer #1 (PuPol1) and mirror M11.
16. Place a fluorescent target into the screw mount in front of the neutral density (ND) filter directly ahead of the parabolic mirror in the beam path. Unblock the pyroelectric power meter that was flipped up in Step 1.
17. Check that the beam is centered on the fluorescent target and adjust M11 if needed. It may be necessary to adjust PuPol1 to allow more power if the beam spot cannot be seen on the target.
18. Readjust PuPol1 back to a lower power. Flip up the power meter to block the beam before removing the target installed in Step 16.
19. Turn on the room lights and proceed.

A.5 Align pump beam spot on the device

With the pump beam path sufficiently aligned, the parabolic mirror is primed to reflect the femtosecond pulse onto the surface of the sample. In order to study the desired physics, specifically nonlinear optical index change in the case of the discussion in Chapter 5, there must be adequate absorption of the pump energy into the dielectric structure. Thus, care must be taken to ensure the pump beam spot on surface of the sample, striking at normal incidence due to the parabolic mirror, is properly aligned to the device under test.

1. Turn on the high-speed Tektronix DPO7254C oscilloscope. Log in to the Windows system built into the tool and wait for the scope software to boot.
2. Ensure that the oscilloscope is being triggered properly by BNC cable carrying a synchronization pulse (clock) for the oscillator repetition rate. Adjust the scale of the oscilloscope waveform to show the leading edge of the clock signal. Use sampling settings that will provide high temporal resolution within this time scale.
3. Rotate PuPol1 to measure a pump energy of 600 nJ/pulse in the pump power meter. This should produce a large enough signal to be measured for alignment without damaging the device.
4. Block the CW probe and unblock the pump by flipping down the pump power meter.
5. The pump beam spot should now be incident on the surface of the sample. You can move it around on the surface within your view in the monitor by adjusting the micrometers of the parabolic mirror M12. Move the beam spot to cover the mark made on the monitor in Step 18 of Section A.3.
6. There should now be a peak in the APD signal as measured in its oscilloscope waveform, occurring near the clock edge seen in Step 2. Sweep the micrometers for the parabolic

mirror and optimize the height of that peak in order to maximize out-of-plane coupling into the device. Note that it is important to always ensure that the end-fire fiber tip alignment to the waveguides is still optimal, as drifting in the fibers could create the false impression that the device is physically behaving differently with respect to the pump signal.

A.6 Adjust fluence & run wavelength sweep

The fluence is a measure of the energy per unit area of the Gaussian beam of the pump and is adjusted by PuPol1 as the first of two crossed polarizers (the other being PuPol2). The experiment being performed might require different pump fluences so attention should be given to the state of PuPol1 and the resulting pulse energy as measured by the pump power meter.

Also, if necessary, the polarization of the pump beam can be adjusted using PuPol2. While it may be necessary to maintain a fixed polarization for the in-plane CW beam to adequately excite the desired waveguide or PhC mode, the out-of-plane pump can vary in polarization rather freely, as there is no "default" polarization for the experiment. This can be adjusted if thought necessary to probe specific physical phenomena, or it can be set to a value that produces a convenient range of fluence values. Bear in mind that by changing the polarization using PuPol2, you are also changing the fluence as defined by the angle between the two crossed polarizer positions. So if the polarization is being changed with PuPol2 and compared to another polarization, it is important to simultaneously change the angle of PuPol1 to ensure the fluence values are comparable. Likewise, changing the polarization could produce a fluence value that is hazardous to the device under test, so it should always be measured with the flip-up power meter before unblocking the beam.

A LabVIEW program is available on the laptop computer at the optics table, written to enable a coordinated sweep between the tunable CW laser (Santec TSL-510) and the high-speed

Tektronix DPO oscilloscope. It communicates with both pieces of equipment, through a blue GPIB connector to interface with the tunable laser and through an ethernet cable to interface with the oscilloscope. The software accepts a range of wavelengths over which to sweep the tunable laser, and at each wavelength step it will record the current waveform being displayed on the oscilloscope. Thus, the settings for the oscilloscope display will directly determine the resolution and scale of the signal data that are recorded. The following steps illustrate how to proceed with a measurement using the sweep program.

1. Check all the connections to and from the laptop computer to ensure everything is connected and interfacing properly.
2. Run the LabVIEW program named "probeWvlSweep_TSL_v11.vi" found on the computer.
3. Specify the sweep start wavelength and number of wavelength steps, along with the step size, to encompass the wavelength range necessary for the experiment at sufficient spectral resolution.
4. Click to run the sweep and confirm at the dialog that the sweep time is reasonable. If the sweep time is too long (e.g., greater than 10 minutes), there is a risk that the fiber tips could drift out of alignment before the sweep is completed. Ensure that the step size resolution is not unnecessarily fine but still sufficient to capture the spectral feature that is being studied.
5. Block the CW probe signal and rerun the same sweep to capture the effect of the pump pulse *alone* on the signal measured at the APD. The pump will couple into the waveguide, travel down it and couple into the fiber to finally be measured at the

oscilloscope, so it is helpful to capture the isolated pump signal, without the probe, in order to have a signal that can be subtracted from the desire data.

6. The sweep files, containing all of the oscilloscope waveforms for each of the number of steps specified, are stored in a dated folder that can be located and copied onto a USB flash drive for later analysis.

A.7 Shutdown procedure

After completing your experiments, take care to power off all the equipment being used and ensure that the lab environment is left in a safe condition for others and yourself. The shutdown procedure will work in reverse from the steps followed for the start-up procedure.

1. Turn off the DC power supply which supplies power to the avalanche photodiode.
2. Power off the high-speed oscilloscope and the pump power meter.
3. Move the fibers away from the sample far enough to safely turn off the piezo controller. When the piezo controller is turned off, the fiber tips will vibrate briefly as the actuators are no longer held at their position.
4. Power off the piezo controller, fiber illuminator, camera, and monitor.
5. Unless leaving the sample mounted on the stage for future experiments, pull back the fibers and slide the brass sample holder out of the stage to unload the sample.
6. Shut down the laptop on the optics table. Ensure that the sweep data is backed up on a flash drive for processing.

After finishing the shutdown of all the upstream components, the Spitfire Ace system should then be shut down to ensure the lifetime and stability of the system. This is done by completing the following steps.

1. Turn the Regen “Off.”
2. Close the Mai-Tai shutter.
3. Click the Mai-Tai “ON/OFF” button.
4. Click the Empower “ON/OFF” button.
5. Exit the Spitfire ACE software.
6. Turn the interlock keys for the Empower and TDG to the “OFF” position.
7. Power down the TDG and TCU controllers.
8. Power down the Empower controller.
9. Turn off the oscilloscope next to the Spitfire Ace system.

References

1. D. A. B. Miller, "Attojoule Optoelectronics for Low-Energy Information Processing and Communications," Journal of Lightwave Technology **35**, 346–396 (2017).
2. G. T. Reed, G. Mashanovich, F. Y. Gardes, and D. J. Thomson, "Silicon optical modulators," Nature Photonics **4**, 518–526 (2010).
3. D. Miller, "Device Requirements for Optical Interconnects to Silicon Chips," Proceedings of the IEEE **97**, 1166–1185 (2009).
4. "3nm Technology - Taiwan Semiconductor Manufacturing Company Limited," https://www.tsmc.com/english/dedicatedFoundry/technology/logic/l_3nm.
5. D. A. B. Miller, "Are optical transistors the logical next step?," Nature Photonics **4**, 3–5 (2010).
6. I. Fushman, D. Englund, A. Faraon, N. Stoltz, P. Petroff, and J. Vučković, "Controlled phase shifts with a single quantum dot," Science **320**, 769–772 (2008).
7. J. L. O'Brien, A. Furusawa, and J. Vučković, "Photonic quantum technologies," Nature Photonics **3**, 687–695 (2009).
8. S. O. Kasap, *Optoelectronics and Photonics: Principles and Practices*, 2nd ed. (Pearson, 2013).
9. J. D. Joannopoulos, S. G. Johnson, J. N. Winn, and R. D. Meade, *Photonic Crystals: Molding the Flow of Light*, 2nd ed. (Princeton University Press, 2008).
10. Q. Quan and M. Loncar, "Deterministic design of wavelength scale, ultra-high Q photonic crystal nanobeam cavities," Optics Express **19**, 18529 (2011).
11. P. B. Deotare, M. W. McCutcheon, I. W. Frank, M. Khan, and M. Lončar, "High quality factor photonic crystal nanobeam cavities," Applied Physics Letters **94**, 121106 (2009).

12. E. M. Purcell, "Spontaneous Emission Probabilities at Radio Frequencies," 839–839 (1995).

13. S. Hu and S. M. Weiss, "Design of Photonic Crystal Cavities for Extreme Light Concentration," ACS Photonics **3**, 1647–1653 (2016).

14. S. Hu, M. Khater, R. Salas-Montiel, E. Kratschmer, S. Engelmann, W. M. J. Green, and S. M. Weiss, "Experimental realization of deep-subwavelength confinement in dielectric optical resonators," Science Advances **4**, eaat2355 (2018).

15. V. R. Almeida, Q. Xu, C. A. Barrios, and M. Lipson, "Guiding and confining light in void nanostructure," Optics Letters **29**, 1209 (2004).

16. J. D. Ryckman and S. M. Weiss, "Low mode volume slotted photonic crystal single nanobeam cavity," Applied Physics Letters **101**, 071104 (2012).

17. P. Seidler, K. Lister, U. Drechsler, J. Hofrichter, and T. Stöferle, "Slotted photonic crystal nanobeam cavity with an ultrahigh quality factor-to-mode volume ratio," Optics Express **21**, 32468 (2013).

18. Q. Quan, P. B. Deotare, and M. Loncar, "Photonic crystal nanobeam cavity strongly coupled to the feeding waveguide," Applied Physics Letters **96**, 203102 (2010).

19. A. Taflove and S. C. Hagness, *Computational Electrodynamics : The Finite-Difference Time-Domain Method*, 3rd ed. (Artech House, 2005).

20. A. Taflove, A. Oskooi, and S. G. Johnson, *Advances in FDTD Computational Electrodynamics : Photonics and Nanotechnology* (Artech House, 2013).

21. Lumerical, ANSYS, Inc., https://www.lumerical.com/

22. A. F. Oskooi, D. Roundy, M. Ibanescu, P. Bermel, J. D. Joannopoulos, and S. G. Johnson, "Meep: A flexible free-software package for electromagnetic simulations by the FDTD method," Computer Physics Communications **181**, 687–702 (2010).

23. Y. Akahane, T. Asano, B.-S. Song, and S. Noda, "High-Q photonic nanocavity in a two-dimensional photonic crystal," Nature **425**, 944–947 (2003).

24. M. W. McCutcheon and M. Lončar, "Design of a silicon nitride photonic crystal nanocavity with a Quality factor of one million for coupling to a diamond nanocrystal," Optics Express **16**, 19136–19145 (2008).

25. B. J. M. Hausmann, B. J. Shields, Q. Quan, Y. Chu, N. P. de Leon, R. Evans, M. J. Burek, A. S. Zibrov, M. Markham, D. J. Twitchen, H. Park, M. D. Lukin, and M. Loncăr, "Coupling of NV Centers to Photonic Crystal Nanobeams in Diamond," Nano Letters **13**, 5791–5796 (2013).

26. F. Liang, N. Clarke, P. Patel, M. Loncar, and Q. Quan, "Scalable photonic crystal chips for high sensitivity protein detection," Optics Express **21**, 32306 (2013).

27. S. Buckley, M. Radulaski, J. L. Zhang, J. Petykiewicz, K. Biermann, and J. Vučković, "Multimode nanobeam cavities for nonlinear optics: high quality resonances separated by an octave," Optics Express **22**, 26498 (2014).

28. Z. Huang, K. Cui, Y. Li, X. Feng, F. Liu, W. Zhang, and Y. Huang, "Strong Optomechanical Coupling in Nanobeam Cavities based on Hetero Optomechanical Crystals," Scientific Reports **5**, 15964 (2015).

29. C. Renaut, B. Cluzel, J. Dellinger, L. Lalouat, E. Picard, D. Peyrade, E. Hadji, and F. de Fornel, "On chip shapeable optical tweezers," Scientific Reports **3**, 2290 (2013).

30. H. Choi, M. Heuck, and D. Englund, "Self-Similar Nanocavity Design with Ultrasmall Mode Volume for Single-Photon Nonlinearities," Physical Review Letters **118**, 223605 (2017).

31. W. H. P. Pernice, C. Xiong, C. Schuck, and H. X. Tang, "High-Q aluminum nitride photonic crystal nanobeam cavities," Applied Physics Letters **100**, 091105 (2012).

32. Y. Chen, W. S. Fegadolli, W. M. Jones, A. Scherer, and M. Li, "Ultrasensitive Gas-Phase Chemical Sensing Based on Functionalized Photonic Crystal Nanobeam Cavities," ACS Nano **8**, 522–527 (2014).

33. P. Shi, G. Zhou, J. Deng, F. Tian, and F. S. Chau, "Tuning all-Optical Analog to Electromagnetically Induced Transparency in nanobeam cavities using nanoelectromechanical system," Scientific Reports **5**, 14379 (2015).

34. P. Yu, H. Qiu, H. Yu, F. Wu, Z. Wang, X. Jiang, and J. Yang, "High-Q and high-order side-coupled air-mode nanobeam photonic crystal cavities in silicon," IEEE Photonics Technology Letters **28**, 2121–2124 (2016).

35. P. Liu and Y. Shi, "Simultaneous measurement of refractive index and temperature using cascaded side-coupled photonic crystal nanobeam cavities," Optics Express **25**, 28398 (2017).

36. S. Hu, Y. Zhao, K. Qin, S. T. Retterer, I. I. Kravchenko, and S. M. Weiss, "Enhancing the Sensitivity of Label-Free Silicon Photonic Biosensors through Increased Probe Molecule Density," ACS Photonics **1**, 590–597 (2014).

37. F. O. Afzal, S. I. Halimi, and S. M. Weiss, "Efficient side-coupling to photonic crystal nanobeam cavities via state-space overlap," Journal of the Optical Society of America B **36**, 585 (2019).

38. P. E. Barclay, K. Srinivasan, M. Borselli, and O. Painter, "Efficient input and output fiber coupling to a photonic crystal waveguide," Optics Letters **29**, 697 (2004).

39. M. Soljačić, S. G. Johnson, S. Fan, M. Ibanescu, E. Ippen, and J. D. Joannopoulos, "Photonic-crystal slow-light enhancement of nonlinear phase sensitivity," Journal of the Optical Society of America B **19**, 2052 (2002).

40. K. Nozaki, T. Tanabe, A. Shinya, S. Matsuo, T. Sato, H. Taniyama, and M. Notomi, "Sub-femtojoule all-optical switching using a photonic-crystal nanocavity," Nature Photonics **4**, 477–483 (2010).

41. B. Ellis, M. A. Mayer, G. Shambat, T. Sarmiento, J. Harris, E. E. Haller, and J. Vučković, "Ultralow-threshold electrically pumped quantum-dot photonic-crystal nanocavity laser," Nature Photonics **5**, 297–300 (2011).

42. K.-Y. Jeong, Y.-S. No, Y. Hwang, K. S. Kim, M.-K. Seo, H.-G. Park, and Y.-H. Lee, "Electrically driven nanobeam laser," Nature Communications **4**, 2822 (2013).

43. M. R. Lee and P. M. Fauchet, "Two-dimensional silicon photonic crystal based biosensing platform for protein detection," Optics Express **15**, 4530 (2007).

44. W.-C. Lai, S. Chakravarty, Y. Zou, Y. Guo, and R. T. Chen, "Slow light enhanced sensitivity of resonance modes in photonic crystal biosensors," Applied Physics Letters **102**, 041111 (2013).

45. S. I. Halimi, Z. Fu, F. O. Afzal, J. A. Allen, S. Hu, and S. M. Weiss, "Photonic Crystal Design with Mix and Match Unit Cells for Mode Manipulation," in *Conference on Lasers and Electro-Optics* (OSA, 2019), p. SM2J.4.

46. H. Choi, D. Zhu, Y. Yoon, and D. Englund, "Cascaded Cavities Boost the Indistinguishability of Imperfect Quantum Emitters," Physical Review Letters **122**, 183602 (2019).

47. P. Lalanne and J. P. Hugonin, "Bloch-wave engineering for high-Q, small-V microcavities," IEEE Journal of Quantum Electronics **39**, 1430–1438 (2003).

48. C. Sauvan, G. Lecamp, P. Lalanne, and J. P. Hugonin, "Modal-reflectivity enhancement by geometry tuning in Photonic Crystal microcavities," Optics Express **13**, 245–255 (2005).

49. S. I. Halimi, S. Hu, F. O. Afzal, and S. M. Weiss, "Realizing high transmission intensity in photonic crystal nanobeams using a side-coupling waveguide," Optics Letters **43**, 4260 (2018).

50. Y. Zhang, S. Yang, A. E.-J. Lim, G.-Q. Lo, C. Galland, T. Baehr-Jones, and M. Hochberg, "A compact and low loss Y-junction for submicron silicon waveguide," Optics Express **21**, 1310 (2013).

51. M. Minkov, V. Savona, and D. Gerace, "Photonic crystal slab cavity simultaneously optimized for ultra-high Q / V and vertical radiation coupling," Applied Physics Letters **111**, 131104 (2017).

52. J. S. Jensen and O. Sigmund, "Topology optimization for nano-photonics," Laser & Photonics Reviews **5**, 308–321 (2011).

53. C. M. Lalau-Keraly, S. Bhargava, O. D. Miller, and E. Yablonovitch, "Adjoint shape optimization applied to electromagnetic design," Optics Express **21**, 21693 (2013).

54. A. Y. Piggott, J. Lu, K. G. Lagoudakis, J. Petykiewicz, T. M. Babinec, and J. Vucković, "Inverse design and demonstration of a compact and broadband on-chip wavelength demultiplexer," Nature Photonics **9**, 374–377 (2015).

55. M. S. Nisar, X. Yang, L. Lu, J. Chen, and L. Zhou, "On-Chip Integrated Photonic Devices Based on Phase Change Materials," Photonics **8**, 205 (2021).

56. R. M. Briggs, I. M. Pryce, and H. A. Atwater, "Compact silicon photonic waveguide modulator based on the vanadium dioxide metal-insulator phase transition," Optics Express **18**, 11192 (2010).

57. M. Rudé, J. Pello, R. E. Simpson, J. Osmond, G. Roelkens, J. J. G. M. Van Der Tol, and V. Pruneri, "Optical switching at 1.55 μm in silicon racetrack resonators using phase change materials," Applied Physics Letters **103**, 141119 (2013).

58. J. D. Ryckman, K. A. Hallman, R. E. Marvel, R. F. Haglund, and S. M. Weiss, "Ultra-compact silicon photonic devices reconfigured by an optically induced semiconductor-to-metal transition," Optics Express **21**, 10753 (2013).

59. C. Wan, Z. Zhang, D. Woolf, C. M. Hessel, J. Rensberg, J. M. Hensley, Y. Xiao, A. Shahsafi, J. Salman, S. Richter, Y. Sun, M. M. Qazilbash, R. Schmidt-Grund, C. Ronning, S. Ramanathan, and M. A. Kats, "On the Optical Properties of Thin-Film Vanadium Dioxide from the Visible to the Far Infrared," Annalen der Physik **531**, 1900188 (2019).

60. Z. Yang, C. Ko, and S. Ramanathan, "Oxide Electronics Utilizing Ultrafast Metal-Insulator Transitions," Annual Review of Materials Research **41**, 337–367 (2011).

61. T. L. Cocker, L. V Titova, S. Fourmaux, G. Holloway, H.-C. Bandulet, D. Brassard, J.-C. Kieffer, M. A. El Khakani, and F. A. Hegmann, "Phase diagram of the ultrafast photoinduced insulator-metal transition in vanadium dioxide," Physical Review B **85**, 155120 (2012).

62. J. B. Kana Kana, J. M. Ndjaka, G. Vignaud, A. Gibaud, and M. Maaza, "Thermally tunable optical constants of vanadium dioxide thin films measured by spectroscopic ellipsometry," Optics Communications **284**, 807–812 (2011).

63. V. R. Morrison, R. P. Chatelain, K. L. Tiwari, A. Hendaoui, A. Bruhács, M. Chaker, and B. J. Siwick, "A photoinduced metal-like phase of monoclinic VO_2 revealed by ultrafast electron diffraction," Science **346**, 445–448 (2014).

64. D. Wegkamp, M. Herzog, L. Xian, M. Gatti, P. Cudazzo, C. L. McGahan, R. E. Marvel, R. F. Haglund, A. Rubio, M. Wolf, and J. Stähler, "Instantaneous Band Gap Collapse in Photoexcited Monoclinic VO_2 due to Photocarrier Doping," Physical Review Letters **113**, 216401 (2014).

65. A. Sood, X. Shen, Y. Shi, S. Kumar, S. J. Park, M. Zajac, Y. Sun, L.-Q. Chen, S. Ramanathan, X. Wang, W. C. Chueh, and A. M. Lindenberg, "Universal phase dynamics in VO_2 switches revealed by ultrafast operando diffraction," Science **373**, 352–355 (2021).

66. P. Markov, R. E. Marvel, H. J. Conley, K. J. Miller, R. F. Haglund, and S. M. Weiss, "Optically Monitored Electrical Switching in VO_2," ACS Photonics **2**, 1175–1182 (2015).

67. K. J. Miller, K. A. Hallman, R. F. Haglund, and S. M. Weiss, "Silicon waveguide optical switch with embedded phase change material," Optics Express **25**, 26527 (2017).

68. K. A. Hallman, A. Baydin, K. J. Miller, S. M. Weiss, and R. F. Haglund, "Ultrafast optical switching of femtosecond 1550 nm pulses in silicon modulators (Conference Presentation)," in *Silicon Photonics XV*, G. T. Reed and A. P. Knights, eds. (SPIE, 2020), Vol. 11285, p. 12.

69. K. A. Hallman, K. J. Miller, A. Baydin, S. M. Weiss, and R. F. Haglund, "Sub-Picosecond Response Time of a Hybrid VO_2:Silicon Waveguide at 1550 nm," Advanced Optical Materials **9**, 2001721 (2021).

70. K. Liu, S. Lee, S. Yang, O. Delaire, and J. Wu, "Recent progresses on physics and applications of vanadium dioxide," Materials Today **21**, 875–896 (2018).

71. Y. Ke, S. Wang, G. Liu, M. Li, T. J. White, and Y. Long, "Vanadium Dioxide: The Multistimuli Responsive Material and Its Applications," Small **14**, 1802025 (2018).

72. S. I. Halimi, Z. Fu, F. O. Afzal, J. A. Allen, S. Hu, and S. M. Weiss, "Controlling the mode profile of photonic crystal nanobeam cavities with mix-and-match unit cells," Journal of the Optical Society of America B **37**, 3401 (2020).

73. K. A. Hallman, "Picosecond Optical Modulation of Vanadium Dioxide Incorporated into Silicon Photonics," Ph.D. dissertation (2018).

74. R. F. Haglund, K. A. Hallman, K. J. Miller, and S. M. Weiss, "Picosecond Optical Switching in Silicon Photonics Using Phase-Changing Vanadium Dioxide," in *Conference on Lasers and Electro-Optics* (OSA, 2019), p. STh4H.1.

75. R. W. Boyd, *Nonlinear Optics*, 3rd ed. (Academic Press, 2008).

76. M. Soljačić and J. D. Joannopoulos, "Enhancement of nonlinear effects using photonic crystals," Nature Materials **3**, 211–219 (2004).

77. M. Notomi, A. Shinya, S. Mitsugi, G. Kira, E. Kuramochi, and T. Tanabe, "Optical bistable switching action of Si high-Q photonic-crystal nanocavities," Optics Express **13**, 2678 (2005).

78. T. Tanabe, M. Notomi, S. Mitsugi, A. Shinya, and E. Kuramochi, "All-optical switches on a silicon chip realized using photonic crystal nanocavities," Applied Physics Letters **87**, 1–3 (2005).

79. T. Tanabe, K. Nishiguchi, A. Shinya, E. Kuramochi, H. Inokawa, M. Notomi, K. Yamada, T. Tsuchizawa, T. Watanabe, H. Fukuda, H. Shinojima, and S. Itabashi, "Fast all-optical switching using ion-implanted silicon photonic crystal nanocavities," Appl. Phys. Lett **90**, 31115 (2007).

80. C. Husko, A. De Rossi, S. Combrí, Q. V. Tran, F. Raineri, and C. W. Wong, "Ultrafast all-optical modulation in GaAs photonic crystal cavities," Applied Physics Letters **94**, 021111 (2009).

81. J. Leuthold, C. Koos, and W. Freude, "Nonlinear silicon photonics," Nature Photonics **4**, 535–544 (2010).

82. L. D. Ryder, K. L. Ryder, A. L. Sternberg, J. A. Kozub, A. Khachatrian, S. P. Buchner, D. Mcmorrow, J. M. Hales, Y. Zhao, L. Wang, C. Wang, R. A. Weller, R. D. Schrimpf, S. M. Weiss, and R. A. Reed, "Simulation of Pulsed-Laser-Induced Testing in Microelectronic Devices," IEEE Transactions on Nuclear Science **68**, 2496–2507 (2021).

83. M. Albrechtsen, B. V. Lahijani, and S. Stobbe, "Two regimes of confinement in photonic nanocavities: bulk confinement versus lightning rods," arXiv:2111.06305 (2021).

84. M. Belotti, M. Galli, D. Gerace, L. C. Andreani, G. Guizzetti, A. R. Md Zain, N. P. Johnson, M. Sorel, and R. M. de La Rue, "All-optical switching in silicon-on-insulator photonic wire nano-cavities," Optics Express **18**, 1450 (2010).